1   March 3, 2023

2

A role for retro-splenial cortex in the task-related P3 network

4

5   **Diptyajit Das[1], Marnie E. Shaw[2], Matti S. Hämäläinen[3,4,5], Andrew R. Dykstra[6], Laura Doll[1],**

6   **and Alexander Gutschalk[1, *]**

7

8   [1] Department of Neurology, Ruprecht-Karls-Universität Heidelberg, Im Neuenheimer Feld 400,

9   69120 Heidelberg, Germany

10   [2] College of Engineering & Computer Science, Australian National University, Canberra, Australia

11   [3] Athinoula A. Martinos Center for Biomedical Imaging, Massachusetts General Hospital, USA

12   [4] Harvard, MIT Division of Health Science and Technology, USA

13   [5] Department of Neuroscience and Biomedical Engineering, Aalto University school of Science,

14   Finland

15   [6] Department of Biomedical Engineering, University of Miami, Coral Gables, USA

16

17   *Corresponding author: Alexander.Gutschalk@med.uni-heidelberg.de

Abstract

The P3 is an event-related response observed in relation to task-relevant sensory events. Despite its ubiquitous presence, the generators of the P3 are controversial and not well identified. Here, we compared source analysis of combined magneto- and electro–encephalography (MEG and EEG) data with fMRI and simulation studies to better understand the sources of the P3 in an auditory oddball paradigm. Our results suggest that the dominant source of the classical, postero-central P3 lies in the retro-splenial cortex of the ventral cingulate gyrus. A second P3 source in the anterior insular cortex contributes little to the postero-central maximum. Multiple other sources in the auditory, somatosensory, and anterior middle cingulate cortex are active in an overlapping time window but can be functionally dissociated based on their activation time courses. These results provide a new perspective for the interpretation of the extensive research based on the P3 response.

Keywords: P300, retro-splenial cortex, insular cortex, EEG, MEG, fMRI, source analysis

Introduction

Many tasks that we perform in response to sensory events recruit widespread cortical networks [Hugdahl et al., 2015; Kim, 2014] as detected by functional magnetic resonance imaging (fMRI). In electroencephalography (EEG), such task-relevant stimuli ubiquitously evoke the prominent P3 [Sutton et al., 1965], also called P300, which has been explored by a large number of cognitive neuroscience studies including such diverse fields as consciousness [Sergent et al., 2005], mental disorders [Hamilton et al., 2020], or brain-computer interfaces [Chaudhary et al., 2016]. Two variants of the P3 have been studied: the earlier P3a is evoked by rare, salient events which are not assigned as target in an active task; it is recorded over more anterior sites in EEG. The later P3b is only observed for task-relevant target events with an amplitude maximum over more posterior sites [Hillyard et al., 1971; Squires et al., 1975]. There are numerous models of the potential psychological processes related to the P3, a summary of which is beyond the scope of this paper [Polich, 2007; Verleger, 2020]. The focus of the present study is on the P3b, but the paradigm used will be expected to evoke some P3a as well, which is why we will refer to the response below simply as P3.

Defining the functional role of the P3 in a neuroanatomically constrained model has been limited by ambiguous findings concerning its neural generators: Early intracranial EEG (iEEG) recordings in patients with epilepsy demonstrated P3-like responses in the hippocampus [Halgren et al., 1980], but subsequent studies in patients with lesions of middle temporal lobe structures demonstrated that the hippocampus is not the source of the P3 as measured by scalp EEG [Johnson, 1988; Onofrj et al., 1992]. Further iEEG studies showed that P3-like responses can be observed by electrodes in many other brain areas [Halgren et al., 1995b; Halgren et al., 1995a], and it was suggested that the neural generator of the P3 is distributed across multiple brain areas, including temporal, frontal, and parietal lobes, as well as the cingulate gyrus. This view was further supported by fMRI, which has been used to constrain source models of the P3 recorded in EEG [Bledowski et al., 2004; Li et al., 2020; Linden et al., 1999; Mulert et al., 2004a; Mulert et al., 2004b]. In

57   agreement with other fMRI studies [Kim, 2014], these constrained source models suggested

58   potential generators of the P3 in the pre-central sulcus (PCS), intra-parietal sulcus (IPS),

59   supplementary motor area (SMA), midcingulate cortex (MCC), insular cortex, and temporo-parietal

60   junction (TPJ). A potential role of the TPJ has been independently emphasized by studies in

61   patients with structural brain lesions [Knight et al., 1989; Verleger et al., 1994; Yamaguchi and

62   Knight, 1991]. Source analysis of the P3 in magnetoencephalography (MEG) has typically

63   suggested sources in the deep [Rogers et al., 1993; Tarkka et al., 1995] temporal lobes, but others

64   reported that the P3 was not obtained reliably at all in MEG [Siedenberg et al., 1996]. Currently, it

65   is widely held that the P3 is generated by the same areas observed active during target detection

66   of rare events in fMRI [Bledowski et al., 2004; Kim, 2014; Mulert et al., 2004b], i.e., in TPJ, dorsal

67   frontal and parietal cortex, and in the MCC and SMA. In other contexts, however, fMRI has been

68   suggested to be linked with gamma activity rather than with evoked potentials in lower frequency

69   bands [Niessing et al., 2005; Steinmann and Gutschalk, 2011], and a detailed investigation of how

70   activity in defined anatomical areas would generate the spatial distribution of the P3 observed in

71   EEG and MEG is still lacking.

72   The present study assessed the neural generators of the P3 by employing combined M/EEG

73   recordings and source analysis in a classical auditory oddball paradigm [Ritter et al., 1972], and

74   directly compared such source analysis results to fMRI. Our results suggest a different source

75   configuration for the P3 than summarized above, with one source lying in retro-splenial cortex

76   (RSC), and another source lying in insular cortex. This P3 activity is paralleled by activity in multiple

77   other areas, including auditory cortex (AC), left primary somato-sensory cortex (S1), and anterior

78   MCC (aMCC), which can be dissociated from the P3 by their activation time courses. In the second

79   part of the paper, we simulated the scalp EEG and sensor MEG distribution based on circumscribed

80   sources in these regions to evaluate (i) their contribution to the centro-parietal P3 that is typically

81   evaluated in EEG, and (ii) to control for the interaction between remote source areas. Finally, we

82   tested which of the simulated sources can explain the data at the P3 peak. Results suggest that

83   the source in RSC explains more variance of the data than other sources.

4

Materials and Methods

Participants

A total of fifteen healthy young adults (female, 8; male 7) with a mean age of 26.8 years (range 20 - 45) with no previous history of neurological or hearing disorder participated in this study. This sample size was based on experience from previous studies using similar source analysis techniques. The data of three participants were excluded later from the analysis due to large measurement artifacts (n=2) and incomplete recording (n=1). The study was approved by the ethics committee of Heidelberg University, Germany and each volunteer provided written informed consent before participation.

Experimental design and procedure

Simultaneous M/EEG data were recorded while presenting a classical auditory oddball sequence consisting of frequent standard (1000 Hz) and rare (14%) deviant (900 Hz) tones. fMRI data were recorded using the same stimuli within a separate session. Tones of 75 ms duration were presented with an average 2-s inter-stimulus interval, randomly jittered by ± 0.5s. A total of 1274 tones were presented across 3 separate runs. Listeners were instructed to press a button with their right index finger to identify all deviant tones. For both M/EEG and fMRI measurements, participants were presented with the same stimuli, with a short break in between the three runs. In MEG, stimuli were presented diotically with ER-3 earphones (Etymotics Research, Elk Grove Village, IL, USA) via foam earpieces. In fMRI, stimuli were presented diotically via MR-compatible S14 insert earphones (Sensimetrics Corporation, Gloucester, MA, USA), which attenuate the scanner noise by approximately 15-20dB. Sound level was individually adjusted to be at a comfortable listening level. All sound stimuli were generated using PsychoPy software (www.psychopy.org) [Peirce, 2007].

Data acquisition

MEG data were acquired at a sampling rate of 1000 Hz (using a 330 Hz online low-pass filter) inside a four-layer magnetically shielded room (IMEDCO) via a Neuromag-122 whole-head system

109 (MEGIN OY, Helsinki, Finland) equipped with 61 dual-channel planar first-order gradiometers.

110 Participants' head geometry and location of four head-position indicator coils were digitized

111 together with the EEG electrode positions relative to a coordinate system spanned by the nasion

112 and two pre-auricular points using a Polhemus Isotrack II digitizer (Colchester, VT, USA). EEG data

113 were recorded using an Easycap (Herrsching, Germany) M64 recording cap with a 64-channel

114 10%-system montage. The EEG was amplified with two 32-channel Neuroscan amplifiers,

115 referenced to Pz, and digitized together with the MEG.

116 MRI data were acquired with a 3T Siemens Magnetom Trio scanner (Siemens Medical Systems,

117 Erlangen, Germany) with a 32-channel coil; fMRI data were acquired with an interleaved echo

118 planar imaging (EPI) sequence (TR=2 sec, TE=30 ms, flip angle 80°) with 32 axial slices aligned

119 along the anterior-posterior commissure line (3.99-mm slices, 3×3 mm^2 in-plane resolution).

120 Structural MRI images with the same field of view were obtained, including T1-weighted anatomical

121 images (GR/MPRAGE, flip angle 9, echo time 2.63, repetition time 1570, resolution 1×1×1 mm^3)

122 and multi-echo fast low-angle shot (FLASH) sequences. These images were used for co-

123 registration with subject-specific M/EEG and fMRI results to standard space and for creating

124 realistic-shaped boundary-element head models. The three scanning runs lasted 800 seconds

125 each and there was a brief break after each run to restart the stimulation and communicate with

126 the participant.

127 **M/EEG data Preprocessing**

128 Preprocessing of M/EEG data was performed using MNE software packages

129 (http://martinos.org/mne) [Gramfort et al., 2013]. For each recording (three runs per participant),

130 first, a visual inspection of the raw M/EEG data was carried out to identify and mark time epochs

131 as well as the channels containing large artifacts or flat signals. A separate denoising was then

132 performed only for the MEG data to reduce uncorrelated sensor noise and artifacts (i.e., flux jumps)

133 using oversampled temporal projection (OTP) [Larson and Taulu, 2018]. This technique allows

134 suppression of sensor-space noise that is spatially uncorrelated with the data. After applying a

135 bandpass filter (0.5-30 Hz) on the M/EEG data, re-referencing of the EEG was performed to an

136   average reference. Eye blinks and cardiac artifacts were then removed from the data using MNE's

137   independent component analysis algorithm [Hyvärinen, 1999]. Afterwards, the data were epoched

138   from -100 to 1000 ms relative to stimulus onset, yielding two stimulus locked conditions: standard

139   and deviant. A separate epoching window spanning -500 to 500 ms relative to the button press

140   was created to track response-locked brain activity. Thus, three overall data conditions were

141   constructed: standard, deviant, and response-locked. Next, the bad segments of epochs (trials)

142   were repaired using an automatic data driven autoreject [Jas et al., 2017] algorithm implemented

143   in MNE. All remaining deviant and response-locked conditions were included in the average

144   response. The number of averaged standards was reduced to the number of deviants using the

145   'mintime' function in MNE, to equalize the number of deviant and standard trials for the source

146   analysis.

147   **The source space and gain matrix**

148   To define an individual, cortically constrained source space, FreeSurfer [Dale et al., 1999; Fischl,

149   2012] was first used to reconstruct the cortical surface (white and pial) from the high-resolution T1-

150   weighted scan (3D MPRAGE data) for each participant. Afterwards, at least 10242 dipoles (i.e.,

151   source locations per hemisphere) were placed at the gray-white matter interface to create the

152   source space, with ~3 mm spacing. The individual forward solution was restricted to a cortical

153   source space parcellation, which excludes corpus callosum and areas below that were removed

154   from the source space. The resulting dipole locations correspond to a cortical surface area of about

155   10 mm^2 on average. High resolution inner-skull, outer-skull, and scalp surfaces created from

156   FLASH images were used to model the electrical conductivity between each surface using a three-

157   compartment boundary-element model (BEM) using MNE. For BEM, 5120 triangles were used for

158   creating the triangulated meshes with respective conductivities of the brain, skull, and skin were

159   assumed to be 0.3 S/m, 0.06 S/m and 0.3 S/m. To define the locations of the EEG electrodes on

160   the scalp and the configuration of the MEG sensors relative to the cortical surface, MNE-coordinate-

161   system alignment tools [Gramfort et al., 2013] were used, where fiducial landmarks (two pre-

162   auricular points and the nasion) are manually identified from the MRI-based rendering of the head

163   surface [Besl and McKay, 1992]. The tool calculates a transformation by minimizing the digitized

164   scalp surface points with respect to the MRI-defined scalp.

165   **Inverse modeling and source analysis of M/EEG data**

166   The field distribution y(t) of sensor/electrode space M/EEG data can be modeled as a linear

167   combination of the source time courses x(t*)* and noise n(t):

168    $$y(t) = Gx(t) + n(t) \qquad (1)$$

169   where, G is the forward gain matrix. To estimate the source current density on the cortical surface

170   for each participant, a separate forward solution for each experimental segment was computed in

171   MNE separately and averaged together [Gramfort et al., 2013; Hämäläinen and Sarvas, 1989;

172   Uutela et al., 2001] for more accurate source estimation. The inverse estimation of active sources

173   (x) is then performed by applying an inverse operator (G´) to the data by using the linear L2

174   minimum-norm estimator (MNE) such that:

175    $$x´ = G´_{MNE}\, y = G^T(GG^T + \lambda^2 C)^{-1}\, y \qquad (2)$$

176   where, x´ is an estimation of the true sources x, C is the noise covariance matrix at the

177   sensor/electrode space, and λ is the Tikhonov regularization parameter. In addition to that, a loose

178   orientation constraint of 0.2 was added to the model so that it can remain flexible against co-

179   registration errors [Lin et al., 2006a] Afterwards, the source estimates were normalized to yield a

180   dSPM [Dale et al., 2000]. This step was performed for each condition (i.e., standard, deviant,

181   deviant - standard, and button response) separately. The noise-covariance matrix was calculated

182   from pre-stimulus baseline i.e., 100 ms preceding the stimuli by using an automated advanced

183   regularization method called shrinkage technique [Engemann and Gramfort, 2015]. Subsequently,

184   noise-normalized source-space data from each participant were transformed onto a template brain

185   atlas i.e., the FreeSurfer average brain (fsaverage) using a spherical registration method [Fischl et

186   al., 1999]. This registration was used to accurately align the dSPM results across individuals. The

187   resulting maps across participants were then averaged per evoked condition to create a single

188   grand-average dSPM solution. For the ROI-based analysis, hand-drawn ROIs were defined on the

189   FreeSurfer average brain based on the anatomy and were then transformed to the individual brain

190   anatomy; ROIs were placed on one side of a sulcus and not across sulci, such that most dipoles

191   within the ROI are expected to have similar dipole orientation and thus polarity. Time-courses per

192   condition were then calculated as average across all dipoles within each ROI, separately for each

193   individual participant. Note that defining a one-polarity ROI for Heschl's gyrus can be complex,

194   because there is often a polarity reversal towards Heschl's sulcus (between Heschl's gyrus and

195   planum temporale). We therefore also explored separate ROIs for the anterior and posterior half of

196   Heschl's gyrus. Because these ROIs revealed similar results for the data of this study, we restricted

197   our analysis to a single ROI defined for the middle of Heschl's gyrus, avoiding the posterior border

198   towards Heschl's sulcus and the anterior border towards the circular sulcus.

199   **Spread analysis of M/EEG data**

200   The point-spread function (PSF) and cross-talk function (CTF) [Hauk et al., 2011] were computed

201   in order to characterize the leakage of current estimates between different ROIs. First, the dSPM-

202   based resolution matrix was computed by multiplying the inverse operator to the forward gain

203   matrix for each ROI. Afterwards, each ROI based PSF and CTF was extracted as the column and

204   the row of that resolution matrix, respectively. This step was then repeated for all individual data

205   set before averaging across participants. Finally, leakage of current estimates and the potential

206   influence of one ROI to another were calculated as the absolute correlation between ROIs for PSFs

207   and CTFs.

208   **Statistical tests and reproducibility**

209   The statistical difference among ROI-based source-level time courses between standards and

210   deviants was assessed through a two-sample cluster-based permutation test [Maris and

211   Oostenveld, 2007] across participants. The statistical test is a non-parametric test that is designed

212   to solve the multiple comparisons problem (MCP) during hypothesis testing. In detail, first, an F

213   statistic is computed at each participant-specific ROI-based source-space data sample (every 2 ms

214   from -100ms to 1000ms relative to stimulus onset) from each data condition. A cluster threshold (p

215   < 0.01) drawn from a standard F distribution was then applied at each sample, keeping only the

216   statistically significant samples to form clusters whose values were higher than the applied

217   threshold. Afterwards, the cluster-level statistic is defined within each cluster by taking the sum of

218   its absolute test statistics. Then, a maximum cluster-level permutation distribution was constructed

219   by using the cluster statistics computed under a Monte Carlo estimation [Ernst, 2004] with random

220   shuffling and 100001 iterations. Cluster level p-values were estimated by computing the proportion

221   that resulted in some larger cluster-level statistics than the actual one calculated from the maximum

222   cluster-level permutation distribution. Significant cluster p-values were defined by correcting the p-

223   values using a Bonferroni correction i.e., critical alpha level (α = 0.05) was set to (α*= α/n <0.0025,

224   where n=20; 10 ROIs x both hemispheres).

225   **fMRI data processing**

226   For each participant, the functional volumes were mapped on the high-resolution anatomical

227   surfaces using FreeSurfer. Surface-based fMRI data processing was then carried out using a

228   standard FS-FAST routine (FreeSurfer's functional analysis stream tool) [Fischl, 2012]. First,

229   preprocessing of the fMRI data was performed that includes the following sequence: template and

230   brain-mask creation, followed by the registration of the functional data with FreeSurfer anatomical

231   structure, motion correction, slice timing correction, intensity normalization of all voxels and time

232   points, resampling of the data to the FreeSurfer average brain (fsaverage) atlas, and spatial

233   smoothing of the data by a 5mm Full-Width/Half-Max (FWHM). Next, first level time series analysis

234   of the data was performed for each participant to remove nuisance variables (i.e., head motion)

235   before computing p-values for a contrast between deviant and standard experimental conditions

236   based on individual participant's time courses with a canonical SPM hemodynamic response

237   function. Later, a random-effects group analysis was performed across participants by using a

238   Generalized Linear Model (GLM) implemented in FreeSurfer [Fischl, 2012], followed by a multiple

239   comparisons correction with the false-discovery rate (FDR, p<0.05) [Genovese et al., 2002]

240   method. fMRI data processing steps were carried out for the left hemisphere and right hemisphere

241   separately.

242 **Cortical M/EEG source simulations**

243 Bilateral, anatomically constrained sources were simulated for each participant's cortical surface

244 mainly based on the ROI already used for the time-course analysis. First, each ROI defined on the

245 FreeSurfer average brain was transformed to the individual brain anatomy. For each anatomical

246 ROI, all dipolar sources lying within were uniformly activated with a time-course of a half-sinusoidal

247 wave composed with a base frequency of 5 Hz. The amplitude of each individual dipole was then

248 scaled such that the absolute value summed over all dipoles within a single ROI amounted to 25

249 nAm peak. The polarity of the sources was assigned as positive- or negative-going for each

250 ROI with reference to the cortical surface. For each ROI, a source in the left and right hemisphere

251 were combined to yield a bilateral source configuration. Only for S1, the simulation was limited to

252 a source in the left hemisphere. To simulate realistic sensor level noise, the individual noise-

253 covariance matrices based on the M/EEG data were used and scaled to a number of 200 averages.

254 The simulations were then analyzed as described above for the experimental data, separately for

255 each ROI used for the simulation. Individual scalp-EEG, sensor-MEG, and cortical dSPM source

256 estimates were computed at the peak of the simulated source for each individual data set and then

257 averaged across all 12 simulated data sets.

258 **Explaining experimental data by simulated activity**

259 Linear combinations of the simulated M/EEG patterns from the previous paragraph were used to

260 explain the scalp/sensor-level M/EEG data. The M/EEG data were averaged across subjects at the

261 individual peak latency of the P3 in EEG electrode Pz and in Cz for the N1. The relative weighting

262 of each simulated ROI component was determined with a least-squares procedure to best explain

263 the M/EEG data. This can be written as:

264 $$\text{Simulated M/EEG} = \arg\min \left(\Sigma_i W_i\, x_i(n) - y(n) \right)^2 \qquad (3)$$

265 Where, W is the latent weighting vector for each (bilateral) ROI, x(n) is the ROI-based M/EEG

266 simulation, and y(n) is the P3 (N1) data.

267   For this procedure, the MEG and EEG data were normalized relative to the standard deviation and

268   mean of the pre-stimulus baseline interval (i.e., MEG and EEG data were transformed to a z score),

269   keeping the relative amplitudes within MEG and EEG data intact. To control for linear dependence,

270   a multi-collinearity test was carried out by calculating the variance-inflation factor (VIF) across the

271   ROI-based M/EEG simulations. VIF cutoff for linear independence was set to 5, i.e., all ROI

272   combinations with a VIF value of less than 5 were considered linearly independent.

273   To quantify the quality of each model, the residual variance (RV) was calculated between the P3

274   (N1) data and the weighted combination of ROI-based simulations. The weights provided in the

275   table represent the weight W multiplied by 25 nAm, which was the strength of the summed

276   simulated activity within each source. In this scaling, the weights provide a rough estimate of the

277   source strength underlying the activity in the respective ROIs at the P3 (N1) peak latency. Note

278   that this source strength does not equal the strength of a single dipolar source, since the variable

279   geometry of ROIs cause different degrees of signal cancelation within each multi-dipole source.

280

Results

282   A standard auditory oddball paradigm was used with the main goal of providing a high signal-to-

283   noise ratio for source analysis. The paradigm comprised repeated, frequent 1000 Hz standard

284   tones and rare 900 Hz deviants, which participants detected by button press. The average hit rate

285   across subjects in M/EEG was 97±3% and mean reaction time 507±103ms (mean ± standard

286   deviation). In fMRI the hit rate was 99±4% and the reaction time 490±150ms.

287   At the electrode and sensor levels (Figure 1a), the two most prominent peaks of the event-related

288   response are the central negativity around 100 ms (N1) in both deviants and standards, and the

289   prominent centro-posterior positivity around 400 ms (P3) evoked by deviants (targets). While this

290   P3 is readily evident as the biggest response in the EEG deviant waveforms around 400 ms, the

291   N1 is more prominent in MEG. When averaging is aligned to the onset of the button press instead

292   (Figure 1b), the EEG shows a slow and steady increase up to about 40 ms after the button press,

293   whereas MEG activity shows a steeper increase right after this event. Thereafter, EEG and MEG

294   similarly show a slow and steady decrease. Maps of the EEG and MEG distribution at the individual

295   maximum at Pz are highly similar when compared between the stimulus- and response-locked

296   versions of the P3, with some differences in the left hemisphere that are more prominent in MEG

297   (Figure 1c).
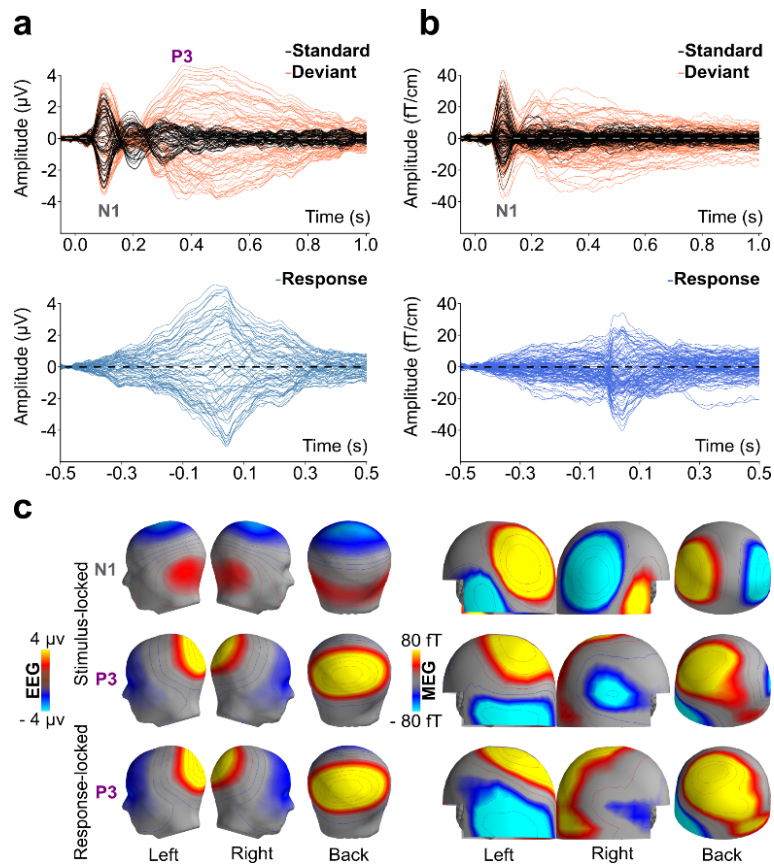
298

299   **Figure 1** Grand-average evoked-response waveforms and maps. (a) Stimulus-locked EEG waveforms (left)

300   and MEG waveforms (right) for standards (black) and deviants (orange). While the N1 is observed for

301   standards and deviants alike, activity in the P3 time window from 300 – 600 ms is only observed for deviants.

302   (b) Waveforms averaged to the button press for detected deviants. While the EEG (left) is dominated by an

303   increasing signal slightly beyond the button press, the MEG (right) shows a particularly strong, steeply rising

304   response after the button press, corresponding to the somato-sensory feedback. c Grand average EEG maps

305   (upper) and reconstructed MEG magnetometer maps (lower) at the peak latency of the N1 (left), the P3

306 (middle), and the response-locked P3 (right). Individual peak latencies for mapping were determined at

307 electrode Cz for N1 and at electrode Pz for response-locked P3.

308

309 **Source analysis of the P3 in comparison to fMRI**

310
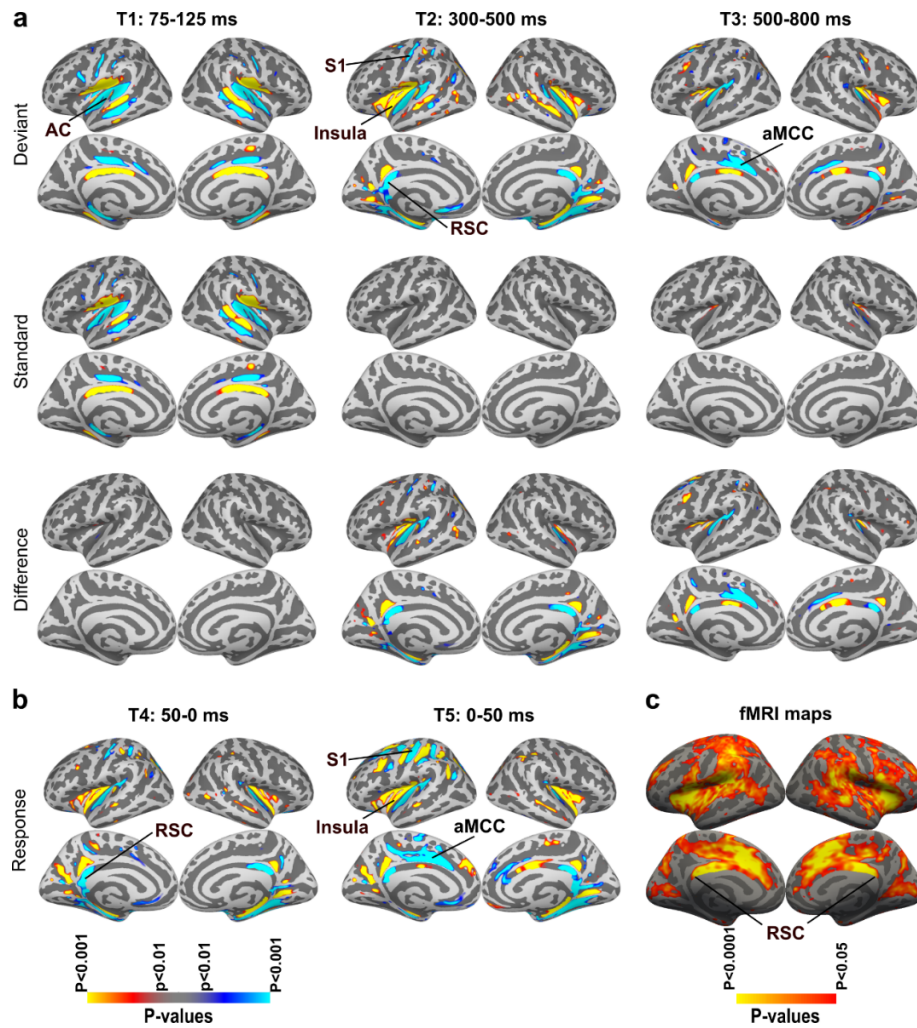
311

312 **Figure 2** Cortical M/EEG and fMRI activation maps. (a) Combined M/EEG dSPM maps for deviants (upper),

313 standards (middle), and the contrast deviants – standards (lower) in three different time windows (p<0.01).

314 The early 75 – 125 ms time window (T1) is focused on the N1, the middle 300 – 500 ms time window (T2) on

315 the P3, and the late 500 – 800 ms time window (T3) on the late frontal negativity. Because the dSPM maps

316 are based on a fixed-effects statistic, the number of standard trials was reduced to the number of deviant trials

14

317   for this analysis. (b) dSPM maps for the response-locked average in the time window 50 ms before and 50

318   ms after the button press. (c) fMRI maps for the contrast deviants – standards (p<0.05, FDR corrected), based

319   on a random-effects statistic.

320

321   To obtain reliable source models for the P3, the raw M/EEG data were first meticulously pre-

322   processed to exclude, and model known artifact sources. Source analysis of the evoked response

323   was obtained by calculating dynamical statistical parametric maps (dSPM) [Dale et al., 2000] in an

324   individual cortical source space, and a dSPM across subjects was then calculated after morphing

325   the individual source estimates onto the Freesurfer average brain. The results of this procedure are

326   shown in Figure 2a. In the early N1 time range (T1: 75 – 125 ms), source activity is observed in AC

327   on the superior temporal plane with spread to adjacent and medial areas, including the inferior

328   parietal lobes, superior temporal sulcus, medial temporal lobes, and posterior MCC (pMCC). For

329   deviants, AC activity persists into the P3 time range (T2: 300 – 500 ms), but the activation pattern

330   somewhat changes its distribution and extends more anteriorly towards the insular cortex then.

331   Moreover, consistent activation is observed in the retro-splenial cortex (RSC) and in the posterior

332   cingulate cortex (PCC) [Vogt et al., 1995; Vogt, 2019]. The RSC and PCC are opposite to each

333   other, lying on the ventral and dorsal bank of the cingulate gyrus, respectively. Accordingly, the

334   polarity with respect to the cortical surface is positive in PCC and negative in RSC, suggesting that

335   only one of the two is the biophysical generator. This activity continues into the later time window

336   (T3:500 – 800 ms), in which additional activity is observed in anterior MCC (aMCC; previously

337   subsumed to ACC [Vogt et al., 1995; Vogt, 2019]). This aMCC activity is of opposite orientation to

338   PCC/RSC, i.e., negative in the dorsal and positive in the ventral bank of aMCC. Qualitatively similar

339   source analysis results were also obtained by application of other widely used source estimation

340   methods (Figure S1) including standardized low-resolution brain electromagnetic tomography

341   (sLORETA) [Pascual-Marqui R D, 2002] and the unit-noise gain minimum variance beamformer

342   (Borgiotti-Kaplan beamformer) [Sekihara and Nagarajan, 2008].

343   We also evaluated the activity with respect to the button presses indicating correct target detection

344   (Figure 2b). These response-locked maps overall show similar activation patterns as the stimulus-

345   locked maps in the 50 ms before the button press. In the 50 ms after the button press, as expected,

346   the activity around left S1 is much stronger. No significant motor-cortex activity, peaking before the

347   button press, was observed.

348   The same auditory oddball paradigm was employed in an fMRI experiment, to directly compare

349   M/EEG and fMRI maps. The fMRI results for the deviant-minus-standard contrast (p<0.05, Figure

350   2c) confirmed previous reports [Bledowski et al., 2004; Kim, 2014] of extensive brain activation for

351   oddball, or generally target detection, with activity in frontal, parietal, and temporal lobes, as well

352   as extensive activation in midline structures around MCC and SMA. When comparing the difference

353   maps for M/EEG (Figure 2a) and fMRI (Figure 2c), it becomes evident that only part of the sites

354   identified by fMRI also show significant source activity in M/EEG, including AC, MCC, S1, and

355   probably insular cortex. Strong fMRI activity is also observed in RSC, but not in PCC. Based on

356   this intramodal comparison, it would therefore appear that the M/EEG activity is also more likely

357   generated in RSC. When the fMRI activity is thresholded more conservatively (Figure S2), it

358   appears that the most robust foci of activity are the RSC, aMCC/SMA, insular cortex, auditory

359   cortex, and TPJ. This pattern is quite similar to the M/EEG source analysis, with the exception of

360   TPJ, where no significant activity was observed in the source analysis.

361   **Source time courses of M/EEG**

362   In order to explore the temporal characteristics of the prominent M/EEG sources in more detail, we

363   calculated source-level time courses for regions of interest (ROI) in the RSC, dorsal aMCC, AC

364   (Heschl's gyrus), insular cortex, and the hand area of S1. As can be observed in these stimulus-

365   and response-locked time courses (Figure 3a and Figure 3b), the ROIs segregate a number of

366   distinct neural processes by their timing. Activity in AC shows the typical N1 waveform. Subsequent

367   to the N1, there is a sustained field that is significant in the deviant-minus-standard comparison on

368   the left. Typical P3-like time courses are observed in RSC and insular cortex, and with longer

16

369   latency in aMCC (note that the orientation of the RSC and aMCC sources are opposite to each

370   other and that only the RSC produces a positive-going field at Pz)

371
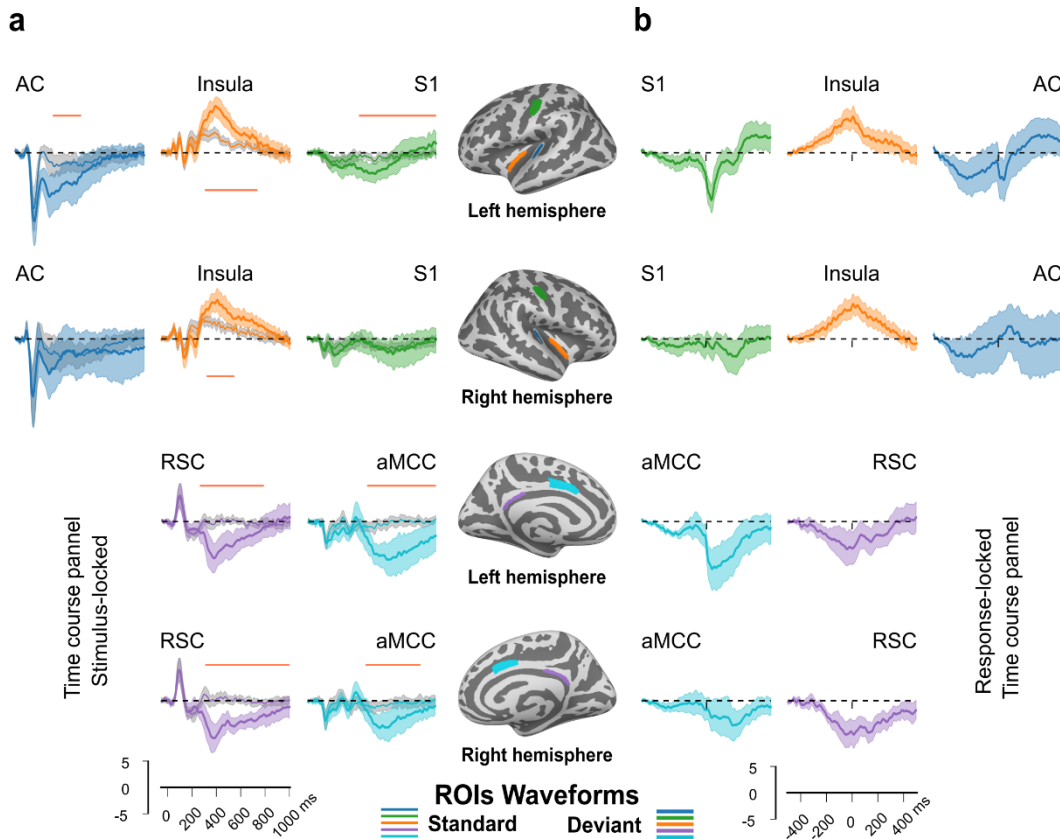
372

373   **Figure 3** ROI-based source waveforms. Source waveforms based on dSPM, calculated for the ROIs shown

374   in the middle column using the same color code. The ROIs include auditory cortex (AC), anterior insular cortex

375   (insula), primary somatosensory cortex (S1), retro-splenial cortex (RSC), and anterior mid cingulate cortex

376   (aMCC). (a) stimulus-locked source time courses, averaged relative to tone onset. Typical P3 source

377   waveforms are observed in RSC (purple) and insula (orange). The orange bar indicates the time interval in

378   which the deviant and standard responses are significantly different from each other (cluster-based

379   permutation test, see methods for details). (b) response-locked source time courses shown in similar

380   configuration.

381

382   An interpretation of the P3 as a build-to-threshold process suggests a response increase until

383   (briefly after) the motor response [O'Connell et al., 2012; Twomey et al., 2015]. The present data

17

384   show a similar response shape directly at the source level in RSC and insular cortex. Note that the

385   stimulus and response locked variants are of approximately similar amplitude, which is compatible

386   with the hypothesis that the P3 is neither locked to the stimulus nor to the response, but represents

387   a mapping between the two [Asanowicz et al., 2020; Verleger et al., 2014]. In contrast, activity in

388   S1 shows a prominent transient wave that peaks approximately 40 ms after the button press, most

389   likely representing tactile and proprioceptive somatosensory feedback related to the button press.

390   A small transient after the button press is also observed in left AC; the latency of this wave coincides

391   with the activity in S1, suggesting that it is spread from or coactivation with S1 rather than auditory

392   evoked activity related to the button press. Finally, activity in aMCC increases rapidly around the

393   button press and persists for more than 300 ms thereafter, suggesting a closer relationship to the

394   task response than to the auditory stimulus.

395   **Comparison with simulated source data**

396   Next, to evaluate the relationship between neural sources, spread of the source estimates, and

397   scalp/sensor distributions, we simulated (i) the source analysis and (ii) the scalp/sensor distribution

398   that would be generated by activity at the different ROIs based on the individual anatomy of the

399   study participants. Each simulated source had a summed source current of 25 nAm (see methods

400   section for details). As expected, these simulations reproduce the spread that is observed for a

401   focal source to neighboring sulci, for example to the inferior parietal lobe and to the superior

402   temporal sulcus in the case of activity in the primary AC (Figure 4a). Spread from AC is also

403   observed in the medial temporal lobe around the hippocampal gyrus and in the pMCC, matching

404   the activity pattern observed at the peak of the N1 in the original data (Figure 2a). This suggests

405   that the data in the 75 - 125 ms time window can be explained with bilateral sources in AC.

406   Some spread is also observed from AC to insular cortex and vice versa. The positive-going activity

407   in insular cortex is not explained by spread from Heschl's gyrus, however, suggesting that this

408   activity observed in the P3 time window is really generated in insular cortex.

409   To quantify the interaction between the evaluated brain regions in the dSPM source analysis, we

410   calculated the point-spread function and cross-talk function between ROIs (Figure 4c; Figure S3

411   and Figure S4). A strong interaction between sources within one hemisphere is observed between

412   (1) Heschl's gyrus and hippocampal gyrus, (2) insular cortex and aMCC, and (3) insular cortex and

413   hippocampal gyrus. Strong spread is also observed between RSC and contralateral aMCC. Spread

414   between left S1 and AC is also confirmed by this analysis, which explains the S1-like waveform for

415   response-looked waveforms in AC (Figure 3a). In contrast, there was comparatively little spread

416   between AC and insular cortex ROIs.
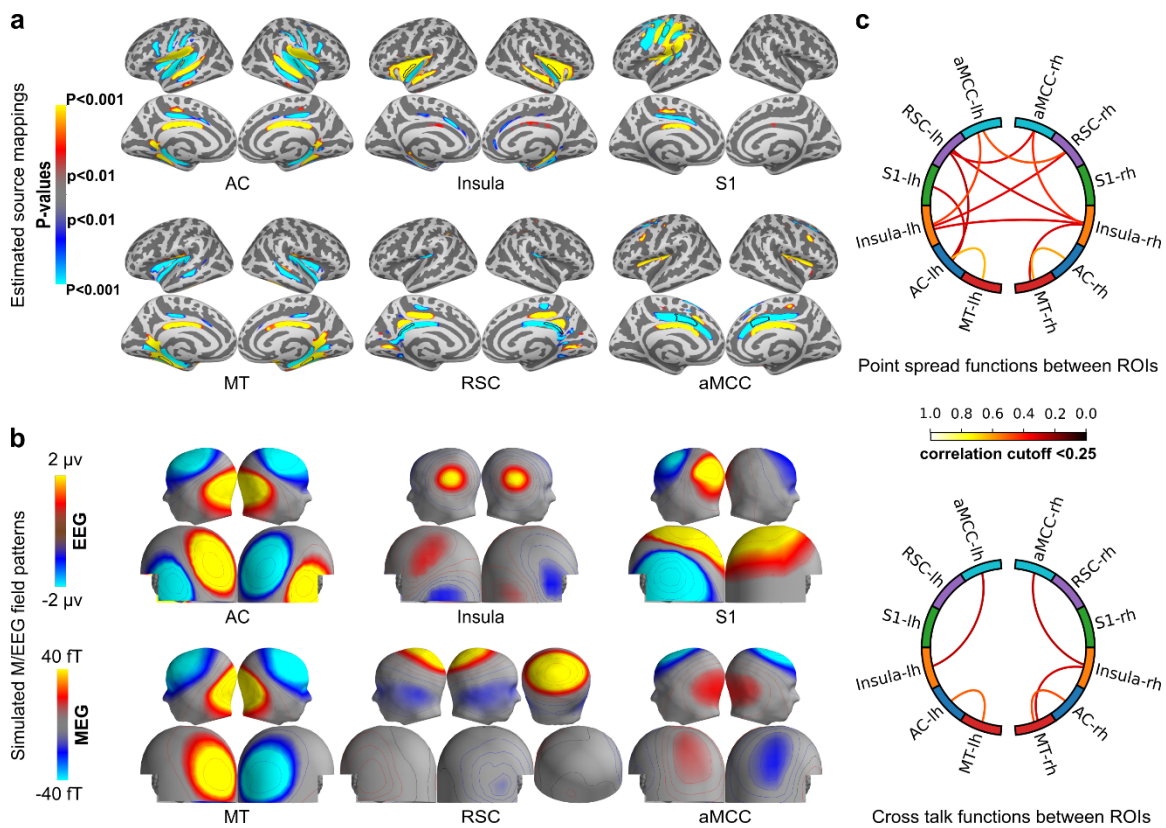
417

418   **Figure 4** Simulated M/EEG and analysis of spread. (a, b) The data represent an average of n=12 individual

419   simulations, based on bilateral, individually morphed ROIs in auditory cortex (AC), Insula, medial temporal

420   cortex (MT), retrosplenial cortex (RSC), and anterior middle cingulate cortex (aMCC). The simulation of the

421   primary sensory hand area (S1) is based on a single, left sided ROI. Source polarity was chosen to match the

422   pattern observed in the N1 (AC, MT) or P3 (insula, S1, RSC, aMCC) time window shown in Figure 2. (a) dSPM

423   based source mappings of the simulated M/EEG data (p<0.01). (b) Scalp/sensor level maps of the grand-

424   average simulated EEG (upper) and MEG (lower), same scaling for all conditions. (c) Point-spread analysis

425   (upper circle) and cross-talk analysis (lower circle) for the same ROIs used in (a) and (b). Each analysis is

19

426 visualized using a circular graph with an absolute arbitrary correlation cutoff value of 0.25. The exact values

427 are summarized in Figure S3 (point spread) and Figure S4 (cross-talk).

428

429 The RSC source produces a symmetric, posterior EEG scalp distribution that matches well with

430 main aspects of the typical P3 observed in our data (Figure 1c). In comparison to EEG, the

431 simulated MEG activity for an RSC source is relatively weak, which could be related to the difficulty

432 of recording P3 in MEG reported previously [Siedenberg et al., 1996]. However, the MEG simulation

433 does not match well with the measured MEG map at the P3 peak (Figure 1c). Moreover, the P3-

434 peak maps showed higher reproducibility in EEG at the individual level, and much more variability

435 in MEG (Supplementary Figures 5 and 6). These data indicate that the explanation of the EEG and

436 in particular the MEG data requires multiple sources, for which MEG and EEG supposedly have

437 different sensitivity.

438 **Explaining the P3 with simulated M/EEG data**

439 We therefore explored how the combined M/EEG P3 data can be explained by a combination of

440 the sources that were used for the time-course analysis. To quantify the relative contribution of

441 potential sources, the simulations based on the ROIs used for the time-course analysis were fitted

442 with a least-squares procedure to the P3 data at its peak. The results show that a reasonable

443 explanation of both EEG and MEG data can be achieved with this procedure (Figure 5), leaving

444 6% residual variance in EEG and 62.5% residual variance in MEG (Table 1). Among all five

445 sources, the RSC was scaled to the highest amplitude. When one of the sources was systematically

446 omitted from the model, a massive increase of residual variance in EEG was only observed with

447 the RSC omitted. Note that omitting RSC also led to the strongest increase of residual variance in

448 MEG, supporting that the relatively weak contribution of the RSC is still relevant for MEG. All other

449 sources only caused weak increment of the residual variance in EEG when omitted. This was also

450 the case for the S1 source, the omittance of which increased the residual variance by only 0.4% in

451 EEG, but by 19% in MEG, demonstrating that this source is almost as important for the MEG maps

452 as the RSC at the P3 peak.

453   To test the validity of the modeling approach, the same sources were fitted to the N1 data, leading

454   to zero weights for all sources except for AC and insula (Figure 5; Table S1). This model resulted

455   in a residual variance of 16.3% in EEG and 27.8% in MEG. While the weighting of the insular cortex

456   of about 1/3 of the auditory cortex appears relatively high, leaving out the insular ROI leads only to

457   a minor increase of the residual variance, whereas the insular cortex alone cannot explain the N1

458   data well.
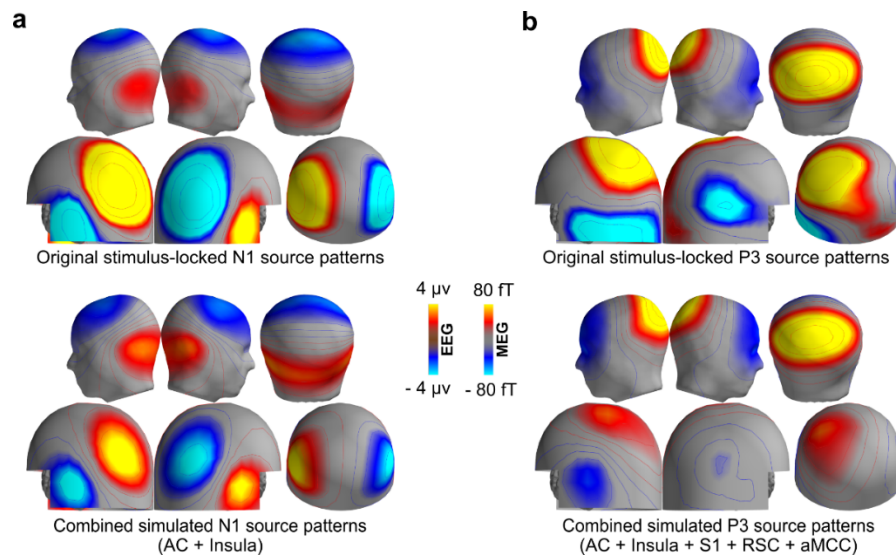
459

460   **Figure 5** Multi-source simulation for the stimulus-locked N1 and P3. (a) Grand average EEG maps and

461   reconstructed MEG magnetometer maps at the peak latency of the N1 in EEG (upper). Combined simulation

462   of N1 maps in scalp/sensor space based on the sum of the sources (AC and insula; see Table S1) fitted to

463   the stimulus-locked N1 (lower). (b) Grand average EEG maps and reconstructed MEG magnetometer maps

464   at the peak latency of the P3 in EEG (upper). Combined simulation of P3 maps in scalp/sensor space based

465   on the sum of the sources (AC, insula, S1, RSC, and aMCC; see Table 1) fitted to the stimulus-locked P3

466   (lower).

467

468   Note that the values of the residual variance of these models must not be directly compared

469   between MEG and EEG. First, higher residual variance in MEG is generally expected based on the

470   more focal signal in planar gradiometers, which leaves other sensors with less signal but similar

471   noise. Second, the relative weighting of MEG and EEG is based on Z-scores, which then results in

21

472 an advantage for EEG because of higher signal to noise level. The relative amplitude of MEG and

473 EEG simulations depends on assumptions made in the head model, in particular the conductivity

474 of the EEG model, which is individually different and difficult to estimate exactly. As a consequence,

475 the amplitude of the MEG is somewhat underestimated by the model, for both N1 and P3, which is

476 an additional source of higher residual variance in MEG compared to EEG.

477

478 **Table 1** Modeling the grand-average P3 data with simulated M/EEG based on anatomically defined

479 source regions (Figure 4b).

	Simulated source activation patterns					Residual variance (RV) (%)	
	AC	Insula	S1	RSC	aMCC	EEG	MEG
Source strength (nAm)	5.50	7.75	11.25	44.25	12.75	6.0	62.50
	-	3.0	12.75	42.0	20.25	6.0	65.30
	3.50	-	11.75	42.0	17.75	5.0	67.0
	9.25	11.25	-	49.75	16.25	6.40	81.50
	0.0	0.0	22.75	-	4.0	52.90	87.10
	10.25	15.50	12.0	45.0	-	8.30	60.50

480

481 Finally, we tested two previous hypotheses for the generation of P3, which were not suggested by

482 the dSPM analysis. First, a source in TPJ has been suggested based on fMRI, fMRI-constrain

483 EEG, and lesion studies [Bledowski et al., 2004; Knight et al., 1989]. To this end, we used the

484 region provided by a standard parcellation [Destrieux et al., 2010]. Such a bilateral TPJ source

485 produces a bilateral posterior maximum (Figure S7b), but cannot replace the RSC in direct

486   comparison. When added as the sixth source to the model from Table 1, TPJ receives no weight.

487   When TPJ is used to replace RSC in a model with five sources, the residual variance increases to

488   50.4% in EEG and 85.4% in MEG, providing no support for a relevant contribution of TPJ to the P3

489   in the present data.

490   Second, a previous EEG study suggested that a distributed source in superior parietal cortex

491   [Moores et al., 2003] could explain the P3. For this simulation, it was assumed that a distributed

492   source existed right below the centro-posterior P3 in the EEG map, extending down to the IPS with

493   a homogeneous amplitude distribution. This extended source indeed produces an EEG pattern with

494   considerable similarity to the centro-posterior P3 (Figure S7b), as well as to the RSC simulation.

495   Replacing the RSC with this distributed source accordingly produces only slightly higher residual

496   variance in comparison (Table S2). It is interesting to note that the dSPM estimate of this simulated

497   source shows considerable spread to the RSC and PCC (Figure S7a), but, conversely, no strong

498   activity in parietal sulci was observed in the P3 source analysis, as would have been predicted by

499   this simulation.

500

Discussion

502   Our results provide evidence of a role for RSC [Vogt et al., 1995; Vogt, 2019] in the generation of

503   the classical P3. A second source with a typical P3 time course was observed in insular cortex, but

504   this component was not dominant for the M/EEG maps. Other sources like S1, AC and aMCC are

505   active in an overlapping time range but contribute to different aspects of the evoked response,

506   which we do not consider part of the classical P3. This model is at odds with the long-held

507   assumption that the P3 as observed by M/EEG is generated by a more distributed set of sources

508   [Bledowski et al., 2004; Mulert et al., 2004b] that is not well accessible to source analysis

509   techniques. The results are based on the combination of EEG, MEG, and individual anatomy to

510   provide the best possible information for the source analysis [Molins et al., 2008]. Conversely, we

511   did not directly constrain the source analysis with information from fMRI [Bledowski et al., 2004]. In

23

512   our view, caution is warranted when using such priors unless correlation between the brain activity

513   measured by the different modalities has been independently confirmed; otherwise, such priors

514   have the potential to mislead M/EEG analyses and lead to incorrect inferences regarding M/EEG

515   sources. Indirectly, however, we used the information provided by fMRI, which first confirms that

516   the RSC is active during target detection, and second allows for the disambiguation of the ventral

517   RSC from the dorsal PCC, an inference that cannot be easily made based on the M/EEG data

518   alone.

519   The limitations of the inverse problem remain, though, and alternative source models can easily be

520   constructed. For example, an extended positive-going source directly below the P3 maximum in

521   the EEG map produced a very similar map and could be used to substitute the RSC source in our

522   model. A previous EEG study that used minimum-norm source reconstruction without noise

523   normalization had proposed such a solution [Moores et al., 2003]. However, the latter method

524   generally prefers superficial sources [Lin et al., 2006b], which is balanced by noise normalization

525   as used in the present study. One further difficulty of M/EEG source analysis is that, in contrast to

526   fMRI, the distribution of a source is not directly related to the actual extent of the activity on the

527   cortex. The pattern with opposite polarity with respect to the (outward) cortical normal in adjacent

528   banks of a sulcus is often caused by spread of a focal source (Figure 4b), whereas a physiological

529   source that extends across both banks with the same polarity would lead to major signal

530   cancelation for distant recordings in M/EEG [Goldenholz et al., 2009]. We therefore chose to display

531   source activity together with polarity information, to avoid the impression of extended sources

532   where they are unlikely, based on the activation pattern, and estimated the spread and activation

533   pattern of each source by simulation studies.

534   The other limitation is the degree to which fMRI can be used to constrain M/EEG source analysis.

535   All sources that were found active in the dSPM maps of this study were also confirmed by fMRI,

536   but fMRI shows activity in additional areas that were not revealed by M/EEG source analysis. There

537   are at least two potential sources for this discrepancy: First, electric activity of similar surface

538   polarity cancels out for M/EEG if the source spans two sides of a sulcus [Ahlfors et al., 2010],

24

539   whereas this configuration would rather support the activity's detection in fMRI. This could e.g.,

540   apply to potential sources in the IPS or TPJ; it could then be that there was another P3 source in

541   this region, but that its signal-to-noise ratio was low for M/EEG. Second, fMRI often does not match

542   with low-frequency M/EEG activity in the delta and theta band such as e.g. the error-related

543   negativity [Agam et al., 2011], but better with neural activity in the gamma band [Logothetis et al.,

544   2001; Niessing et al., 2005; Steinmann and Gutschalk, 2011]. Thus, while the strong RSC activity

545   in fMRI generally supports the RSC's contribution to the P3 source, it still remains possible that the

546   relationship between M/EEG and fMRI activity in this region is indirect, e.g., via functionally coupled

547   gamma activity.

548   Activity in the PCC and RSC has also been reported in intracranial recordings of the P3 [Halgren

549   et al., 1995b], without providing a clear separation between the two. While the authors of that study

550   suggested that the PCC/RSC was a source of the P3a rather than the P3b, neither fMRI [Kim,

551   2014] nor source-analysis studies [Bledowski et al., 2004] have confirmed such a strict separation

552   of P3 subcomponents as suggested based on these intracranial data. As a limitation, while the

553   depth recordings found high amplitudes in and near PCC, no polarity reversal was found [Halgren

554   et al., 1995b], which would have confirmed that the electrode passed through the source.

555   Another constraint for a potential P3 source in RSC is how this region is connected to other brain

556   networks recruited by target processing. The PCC has been demonstrated to be a major hub of the

557   "task-negative" default-mode network [Fox et al., 2005], while activation during oddball detection

558   [Kim, 2014] has been observed in "task-positive" networks [Fox et al., 2005; Hugdahl et al., 2015]

559   such as the dorsal and ventral attention networks [Yeo et al., 2011]. In the early resting-state

560   network studies, PCC activation included all of RSC [Fox et al., 2005], whereas later, more detailed

561   network maps [Yeo et al., 2011] segregated the dorsal part of RSC into a fronto-parietal network,

562   which would better match with a role in active target detection. Anatomical studies in monkeys

563   indicate that both PCC and RSC are reciprocally connected with multiple frontoparietal areas that

564   are active during oddball tasks in fMRI [Kobayashi and Amaral, 2007; Vogt and Pandya, 1987].

565   This would be consistent with the idea that even if the fronto-parietal network does not itself

25

566   generate the P3, it may still be functionally coupled with a generator in RSC. Such connectivity

567   would explain previous findings of reduced P3 with right-TPJ lesions [Knight et al., 1989; Verleger

568   et al., 1994], even if TPJ was not the source of P3. In fact, a model where TPJ provides input into

569   RSC, the neuroelectric source of P3, could better explain why unilateral TPJ lesions caused

570   bilateral reduction of the P3 [Knight et al., 1989].

571   The RSC is also functionally coupled to the hippocampus in the medial temporal lobe [Alexander

572   et al., 2018]. Given the hippocampal P3-like activity demonstrated by iEEG [Halgren et al., 1980],

573   this raises the possibility of a close functional coupling between the extracranial P3 in M/EEG and

574   the intracranial hippocampal activity, despite their anatomical dissociation. Another important

575   question for the source analysis and simulation studies was if hippocampal P3-like activity could

576   potentially be recorded in M/EEG. Despite its clear demonstration in iEEG [Halgren et al., 1980],

577   no hippocampal activity has been shown in fMRI in this (Figure 2c) or previous odd-ball-paradigm

578   fMRI studies [Kim, 2014]. One possible reason for this negative finding could be different neuro-

579   vascular coupling in medial temporal lobe compared to neocortex [Hill et al., 2021], suggested

580   recently based on combined iEEG and fMRI. While the contribution of a hippocampal source to the

581   parietal P3 in EEG had already been excluded based on lesion studies [Johnson, 1988; Onofrj et

582   al., 1992], this does not exclude that hippocampal activity may generally contribute to other aspects

583   of the M/EEG response [Alberto et al., 2021], even though with only a weak signal-to-noise ratio.

584   Indeed, the mapping shown in Figure 2 also suggests activity in the medial temporal lobe. However,

585   this activity was as prominent in the N1 as in the P3 time interval, which is not consistent with

586   known iEEG time courses in hippocampus [Halgren et al., 1980]. Moreover, we demonstrated that

587   there is considerable spread and crosstalk between the medial temporal lobe and AC as well as

588   insular cortex (Figure 4). It is therefore more likely that the activity observed in the medial temporal

589   lobe in our source analysis represents spread from AC and insular cortex, particularly given the

590   fact that M/EEG signal-to-noise ratio is much higher in AC (and somewhat higher in insular cortex)

591   than in the hippocampus [Goldenholz et al., 2009]. This leaves us with the paradoxical situation

592   that there is strong iEEG evidence for P3-like activity in the hippocampus evoked by the paradigm

593   used [Halgren et al., 1980], but that this activity is hard to detect or to distinguish from other sources

594   with all three non-invasive techniques used in this study.

595   The situation is somewhat different for the insula. While there is also spread from AC to the insula

596   (or its vicinity) in the N1 time interval, the pattern is clearly different in the P3 time interval, with

597   surface-positive activity in the insular cortex; activity in AC remains surface negative in this time

598   interval, as reported previously for a passive oddball paradigm [Kretzschmar and Gutschalk, 2010].

599   We therefore consider it more likely that the P3-like time course shown in Figure 3 is generated in

600   the insula, rather than in the temporal lobe. P3 generators in the insula have been suggested

601   before. An EEG study [Bledowski et al., 2004] suggested a contribution of insular cortex to the P3a.

602   A recent iEEG study demonstrated a stronger P3b in anterior insular cortex [Citherlet et al., 2020],

603   in synchrony with gamma activity in the same latency range. Given the observation of strong fMRI

604   activity for detected oddballs in insular cortex, this supports the hypothesis stated above that

605   gamma is a potential link between the P3 and BOLD activity. Finally, strong fMRI activity was

606   observed in aMCC. Insular and aMCC activity are often observed together in fMRI [Yeo et al.,

607   2011], but the time course of the insula and aMCC found here are quite different: the insular time

608   course is similar to the RSC and shows a build-up towards the time of the button press. In contrast,

609   aMCC activity was most prominent after the button press and may thus rather indicate some kind

610   of performance control [Heilbronner and Platt, 2013].

611   At this point, this source analysis is limited to a single paradigm, the classical auditory oddball

612   paradigm. The dominant component in this paradigm is the P3b, but it can be expected that some

613   P3a source activity will also be present. Therefore, we cannot as yet make strong conclusions with

614   respect to the neural sources of these subcomponents. The EEG distribution of the simulated

615   bilateral RSC source over centro-parietal electrodes, however, makes it a better fit for the P3b

616   rather than the P3a [Polich, 2007]. If other sources are more specific for the P3a [Halgren et al.,

617   1995a] or show strong overlap between these two subcomponents [Kim, 2014] will require further

618   studies that manipulate the relative strength of these components. Other, more complex tasks will

619   certainly be expected to involve additional brain regions. While we propose that the P3 generator

620 in RSC will remain a constant contributor for such paradigms as well, this hypothesis requires

621 evaluation in future experiments or the reevaluation of existing data.

622 **Conclusion**

623 Multiple neural processes are active in parallel with the P3 in M/EEG, some observed more easily

624 with fMRI and some more easily with EEG or MEG. But while the P3 is most likely functionally

625 coupled to this distributed neural network, it does not appear to be the bioelectric source of the

626 classical, parietal P3 signal measured in EEG. Based on the evidence presented here, this source

627 appears to be more focal and to lie in the RSC. This finding is essential to explore the functional

628 role of the P3 between the fronto-parietal network observed in fMRI [Kim, 2014] and the

629 hippocampal P3-like activity demonstrated with iEEG [Halgren et al., 1980], and will help to better

630 understand the functional roles of both RSC and the P3. Moreover, understanding its functional

631 anatomy may support the application of the P3 as diagnostic tool. For example, reduced P3 in

632 Alzheimer's disease [Frodl et al., 2002] might be linked to cortical hypometabolism and tau

633 accumulation [Strom et al., 2022], the latter of which has been suggested to covary with the

634 connectivity between RSC and hippocampus [Ziontz et al., 2021]. We hope that future invasive

635 studies will seek to confirm the source configuration suggested by this non-invasive study, possibly

636 by demonstrating co-occurrence of (high-)gamma activity together with a typical P3 time course in

637 RSC.

638

639 **Author contributions**

640 **Diptyajit Das:** Conceptualization, Formal Analysis, Data Curation, Visualization, Writing - Original

641 Draft; **Marnie E. Shaw:** Conceptualization, Investigation, Writing - Review & Editing; **Matti S.**

642 **Hämäläinen:** Validation, Writing - Review & Editing; **Andrew R. Dykstra:** Validation, Writing -

643 Review & Editing; **Laura Doll:** Validation, Writing - Review & Editing; **Alexander Gutschalk:**

644 Conceptualization, Supervision, Validation, Writing - Original Draft & Editing, Funding acquisition.

645

Conflict of interest statement

The authors declare no competing financial interests.

Data availability

The processed M/EEG and fMRI data and scripts will be made available on heiDATA, the open research data repository of Heidelberg University under the following doi (not yet published): https://doi.org/10.11588/data/YB9SQI

References

Agam Y, Hämäläinen MS, Lee AKC, Dyckman KA, Friedman JS, Isom M, Makris N, Manoach DS (2011): Multimodal neuroimaging dissociates hemodynamic and electrophysiological correlates of error processing. Proc Natl Acad Sci U S A 108:17556–17561.

Ahlfors SP, Han J, Lin FH, Witzel T, Belliveau JW, Hämäläinen MS, Halgren E (2010): Cancellation of EEG and MEG signals generated by extended and distributed sources. Hum Brain Mapp 31:140–149. http://www.ncbi.nlm.nih.gov/pubmed/19639553.

Alberto GE, Stapleton-Kotloski JR, Klorig DC, Rogers ER, Constantinidis C, Daunais JB, Godwin DW (2021): MEG source imaging detects optogenetically-induced activity in cortical and subcortical networks. Nat Commun 12:5259. http://dx.doi.org/10.1038/s41467-021-25481-y.

Alexander AS, Rangel LM, Tingley D, Nitz DA (2018): Neurophysiological signatures of temporal

670   coordination between retrosplenial cortex and the hippocampal formation. Behav Neurosci

671   132:453–468.

672   Asanowicz D, Gociewicz K, Marcin K, Finc K, Bonna K, Cleeremans A, Binder M (2020): The

673   response relevance of visual stimuli modulates the P3 component and the underlying

674   sensorimotor network:1–20.

675   Besl PJ, McKay ND (1992): A method for registration of 3D shapes. IEEE Trans Pattern Anal

676   Mach Intell 14:239–256.

677   Bledowski C, Prvulovic D, Hoechstetter K, Scherg M, Wibral M, Goebel R, Linden DEJ (2004):

678   Localizing P300 generators in visual target and distractor processing: a combined event-

679   related potential and functional magnetic resonance imaging study. J Neurosci 24:9353–

680   9360.

681   http://www.ncbi.nlm.nih.gov/entrez/query.fcgi?cmd=Retrieve&db=PubMed&dopt=Citation&li

682   st_uids=15496671.

683   Chaudhary U, Birbaumer N, Ramos-Murguialday A (2016): Brain-computer interfaces for

684   communication and rehabilitation. Nat Rev Neurol 12:513–525.

685   Citherlet D, Boucher O, Tremblay J, Robert M, Gallagher A, Bouthillier A, Lepore F, Nguyen DK

686   (2020): Spatiotemporal dynamics of auditory information processing in the insular cortex: an

687   intracranial EEG study using an oddball paradigm. Brain Struct Funct 225:1537–1559.

688   https://doi.org/10.1007/s00429-020-02072-z.

689   Dale a M, Fischl B, Sereno MI (1999): Cortical surface-based analysis. I. Segmentation and

690   surface reconstruction. Neuroimage 9:179–194.

691   http://www.ncbi.nlm.nih.gov/entrez/query.fcgi?cmd=Retrieve&db=PubMed&dopt=Citation&li

692   st_uids=9931268.

693   Dale AM, Liu AK, Fischl BR, Buckner RL, Belliveau JW, Lewine JD, Halgren E (2000): Dynamic

694   Statistical Parametric Mapping. Neuron 26:55–67.

695   Destrieux C, Fischl B, Dale A, Halgren E (2010): Automatic parcellation of human cortical gyri and

696   sulci using standard anatomical nomenclature. Neuroimage 53:1–15.

697   http://dx.doi.org/10.1016/j.neuroimage.2010.06.010.

698   Engemann DA, Gramfort A (2015): Automated model selection in covariance estimation and

699   spatial whitening of MEG and EEG signals. Neuroimage 108:328–342.

700   http://dx.doi.org/10.1016/j.neuroimage.2014.12.040.

701   Ernst MD (2004): Permutation methods: A basis for exact inference. Stat Sci 19:676–685.

702   Fischl B, Sereno MI, Tootell RBH, Dale a M (1999): High-resolution inter-subject averaging and a

703   surface-based coordinate system. Hum Brain Mapp 8:272–284.

704   Fischl B (2012): FreeSurfer. Neuroimage 62:774–781.

705   Fox MD, Snyder AZ, Vincent JL, Corbetta M, Van Essen DC, Raichle ME (2005): The human

706   brain is intrinsically organized into dynamic, anticorrelated functional networks. Proc Natl

707   Acad Sci U S A 102:9673–8.

708   http://www.pubmedcentral.nih.gov/articlerender.fcgi?artid=1157105&tool=pmcentrez&rende

709   rtype=abstract.

710   Frodl T, Hampel H, Juckel G, Bürger K, Padberg F, Engel RR, Möller HJ, Hegerl U (2002): Value

711   of event-related P300 subcomponents in the clinical diagnosis of mild cognitive impairment

712   and Alzheimer's disease. Psychophysiology 39:175–181.

713   Genovese CR, Lazar NA, Nichols T (2002): Thresholding of statistical maps in functional

714   neuroimaging using the false discovery rate. Neuroimage 15:870–878.

715   Goldenholz DM, Ahlfors SP, Hämäläinen MS, Sharon D, Ishitobi M, Vaina LM, Stufflebeam SM

716   (2009): Mapping the signal-to-noise-ratios of cortical sources in magnetoencephalography

717   and electroencephalography. Hum Brain Mapp 30:1077–1086.

718   Gramfort A, Luessi M, Larson E, Engemann DA, Strohmeier D, Brodbeck C, Goj R, Jas M,

719   Brooks T, Parkkonen L, Hämäläinen M (2013): MEG and EEG data analysis with MNE-

720   Python. Front Neurosci 7:1–13.

721   Halgren E, Baudena P, Clarke JM, Heit G, Liégeois C, Chauvel P, Musolino a (1995a):

722   Intracerebral potentials to rare target and distractor auditory and visual stimuli. I. Superior

723   temporal plane and parietal lobe. Electroencephalogr Clin Neurophysiol 94:191–220.

724   Halgren E, Baudena P, Clarke JM, Heit G, Marinkovic K, Devaux B, Vignal JP, Biraben a

725   (1995b): Intracerebral potentials to rare target and distractor auditory and visual stimuli. II.

726   Medial, lateral and posterior temporal lobe. Electroencephalogr Clin Neurophysiol 94:229–

727   250.

728   Halgren E, Squires NK, Wilson CL, Rohrbaugh JW, Babb TL (1980): Endogenous potentials

729   generated in the human hippocampal formation and amygdala by infrequent events.

730   Science (80-) 210:803–805.

731   Hämäläinen MS, Sarvas J (1989): Realistic conductivity geometry model of the human head for

732   interpretation of neuromagnetic data. IEEE Trans Biomed Eng 36:165–171.

733   http://www.ncbi.nlm.nih.gov/entrez/query.fcgi?cmd=Retrieve&db=PubMed&dopt=Citation&li

734   st_uids=2917762.

735   Hamilton HK, Boos AK, Mathalon DH (2020): Electroencephalography and Event-Related

736   Potential Biomarkers in Individuals at Clinical High Risk for Psychosis. Biol Psychiatry

737   88:294–303. https://doi.org/10.1016/j.biopsych.2020.04.002.

738   Hauk O, Wakeman DG, Henson R (2011): Comparison of noise-normalized minimum norm

739   estimates for MEG analysis using multiple resolution metrics. Neuroimage 54:1966–1974.

740   http://dx.doi.org/10.1016/j.neuroimage.2010.09.053.

741   Heilbronner SR, Platt ML (2013): Causal evidence of performance monitoring by neurons in

742   posterior cingulate cortex during learning. Neuron 80:1384–1391.

743   http://dx.doi.org/10.1016/j.neuron.2013.09.028.

744   Hill PF, Seger SE, Yoo H Bin, King DR, Wang DX, Lega BC, Rugg MD (2021): Distinct

745   neurophysiological correlates of the fMRI BOLD signal in the hippocampus and neocortex. J

746   Neurosci 41:6343–6352.

747   Hillyard SA, Squires KC, Bauer JW, Lindsay PH (1971): Evoked potential correlates of auditory

748   signal detection. Science 172:1357–1360.

749   http://www.ncbi.nlm.nih.gov/entrez/query.fcgi?cmd=Retrieve&db=PubMed&dopt=Citation&li

750   st_uids=5580218.

751   Hugdahl K, Raichle ME, Mitra A, Specht K (2015): On the existence of a generalized non-specific

752   task- dependent network. Front Hum Neurosci 9:1–15.

753   Hyvärinen A (1999): Fast and robust fixed-point algorithms for independent component analysis.

754   IEEE Trans Neural Networks 10:626–634.

755   Jas M, Engemann DA, Bekhti Y, Raimondo F, Gramfort A (2017): Autoreject: Automated artifact

756   rejection for MEG and EEG data. Neuroimage 159:417–429.

757   https://doi.org/10.1016/j.neuroimage.2017.06.030.

758   Johnson R (1988): Scalp-recorded p300 activity in patients following unilateral temporal

759   lobectomy. Brain 111:1517–1529.

760   Kim H (2014): Involvement of the dorsal and ventral attention networks in oddball stimulus

761   processing: A meta-analysis. Hum Brain Mapp 35:2265–84.

762   http://www.ncbi.nlm.nih.gov/pubmed/23900833.

763   Knight RT, Scabini D, Woods DL, Clayworth CC (1989): Contributions of temporal-parietal

764   junction to the human auditory P3. Brain Res 502:109–116.

765   Kobayashi Y, Amaral DG (2007): Macaque monkey retrosplenial cortex: III. cortical efferents. J

766   Comp Neurol 502:810–833.

767   Kretzschmar B, Gutschalk A (2010): A sustained deviance response evoked by the auditory

768   oddball paradigm. Clin Neurophysiol 121.

769   Larson E, Taulu S (2018): Reducing Sensor Noise in MEG and EEG Recordings Using

770   Oversampled Temporal Projection. IEEE Trans Biomed Eng 65:1002–1013.

771   Li F, Tao Q, Peng W, Zhang T, Si Y, Zhang Y, Yi C, Biswal B, Yao D, Xu P (2020): Inter-subject

772   P300 variability relates to the efficiency of brain networks reconfigured from resting- to task-

773   state: Evidence from a simultaneous event-related EEG-fMRI study. Neuroimage

774   205:116285. https://doi.org/10.1016/j.neuroimage.2019.116285.

775   Lin FH, Belliveau JW, Dale AM, Hamalainen MS (2006a): Distributed current estimates using

776   cortical orientation constraints. Hum Brain Mapp 27:1–13.

777   http://www.ncbi.nlm.nih.gov/entrez/query.fcgi?cmd=Retrieve&db=PubMed&dopt=Citation&li

778   st_uids=16082624.

779   Lin FH, Witzel T, Ahlfors SP, Stufflebeam SM, Belliveau JW, Hamalainen MS (2006b): Assessing

780   and improving the spatial accuracy in MEG source localization by depth-weighted minimum-

781   norm estimates. Neuroimage 31:160–171.

782   http://www.ncbi.nlm.nih.gov/entrez/query.fcgi?cmd=Retrieve&db=PubMed&dopt=Citation&li

783   st_uids=16520063.

784   Linden DE, Prvulovic D, Formisano E, Vollinger M, Zanella FE, Goebel R, Dierks T (1999): The

785   functional neuroanatomy of target detection: an fMRI study of visual and auditory oddball

786   tasks. Cereb Cortex 9:815–823.

787   http://www.ncbi.nlm.nih.gov/entrez/query.fcgi?cmd=Retrieve&db=PubMed&dopt=Citation&li

788   st_uids=10601000.

789   Logothetis NK, Pauls J, Augath M, Trinath T, Oeltermann a (2001): Neurophysiological

790   investigation of the basis of the fMRI signal. Nature 412:150–157.

791   http://www.ncbi.nlm.nih.gov/entrez/query.fcgi?cmd=Retrieve&db=PubMed&dopt=Citation&li

792   st_uids=11449264.

793   Maris E, Oostenveld R (2007): Nonparametric statistical testing of EEG- and MEG-data. J

794   Neurosci Methods 164:177–190.

795   Molins A, Stufflebeam SM, Brown EN, Hämäläinen MS (2008): Quantification of the benefit from

796   integrating MEG and EEG data in minimum ℓ2-norm estimation. Neuroimage 42:1069–1077.

797   Moores KA, Clark CR, Hadfield JLM, Brown GC, Taylor DJ, Fitzgibbon SP, Lewis AC, Weber DL,

798   Greenblatt R (2003): Investigating the generators of the scalp recorded visuo-verbal P300

799   using cortically constrained source localization. Hum Brain Mapp 18:53–77.

800   Mulert C, Pogarell O, Juckel G, Rujescu D, Giegling I, Rupp D, Mavrogiorgou P, Bussfeld P,

801   Gallinat J, Möller HJ, Hegerl U (2004a): The neural basis of the P300 potential: Focus on

802   the time-course of the underlying cortical generators. Eur Arch Psychiatry Clin Neurosci

803   254:190–198.

804   Mulert C, Jäger L, Schmitt R, Bussfeld P, Pogarell O, Möller HJ, Juckel G, Hegerl U (2004b):

805   Integration of fMRI and simultaneous EEG: Towards a comprehensive understanding of

806   localization and time-course of brain activity in target detection. Neuroimage 22:83–94.

807   Niessing J, Ebisch B, Schmidt KE, Niessing M, Singer W, Galuske R a W (2005): Hemodynamic

808   signals correlate tightly with synchronized gamma oscillations. Science (80-) 309:948–951.

809   http://www.ncbi.nlm.nih.gov/entrez/query.fcgi?cmd=Retrieve&db=PubMed&dopt=Citation&li

810   st_uids=16081740.

811   O'Connell RG, Dockree PM, Kelly SP (2012): A supramodal accumulation-to-bound signal that

812   determines perceptual decisions in humans. Nat Neurosci 15:1729–1735.

813   Onofrj M, Fulgente T, Nobilio D, Malatesta G, Bazzano S, Colamartino P, Gambi D (1992): P3

814   recordings in patients with bilateral temporal lobe lesions. Neurology 42:1762–1767.

815   Pascual-Marqui R D (2002): Standardized low resolution brain electromagnetic tomography

816   (sLORETA): technical details. Methods Find Exp Clin Pharmacol 24:5–12.

817   http://www.keyinst.unizh.ch/loreta.htm.

818   Peirce JW (2007): PsychoPy-Psychophysics software in Python. J Neurosci Methods 162:8–13.

819   http://dx.doi.org/10.1016/j.jneumeth.2006.11.017.

820   Polich J (2007): Updating P300: An integrative theory of P3a and P3b. Clin Neurophysiol

821   118:2128–2148.

822   Ritter W, Simson R, Vaughan HG (1972): Association cortex potentials and reaction time in

823   auditory discrimination. Electroencephalogr Clin Neurophysiol 33:547–555.

824   Rogers RL, Basile LFH, Papanicolaou AC, Eisenberg HM (1993): Magnetoencephalography

825   reveals two distinct sources associated with late positive evoked potentials during visual

826   oddball task. Cereb Cortex 3:163–169.

827   Sekihara K, Nagarajan SS (2008): Adaptive Spatial Filters for Electromagnetic Brain Imaging.

828   Series in. Springer, Berlin; Heidelberg.

829   Sergent C, Baillet S, Dehaene S (2005): Timing of the brain events underlying access to

830   consciousness during the attentional blink. Nat Neurosci 8:1391–1400.

831   Siedenberg R, Goodin DS, Aminoff MJ, Rowley HA, Roberts TPL (1996): Comparison of late

832   components in simultaneously recorded event-related electrical potentials and event-related

833   magnetic fields. Electroencephalogr Clin Neurophysiol 99:191–197.

834   Squires NK, Squires KC, Hillyard SA (1975): Two varieties of long-latency positive waves evoked

835   by unpredictable auditory stimuli in man. Electroencephalogr Clin Neurophysiol 38:387–401.

836   http://www.ncbi.nlm.nih.gov/entrez/query.fcgi?cmd=Retrieve&db=PubMed&dopt=Citation&li

837   st_uids=46819.

838   Steinmann I, Gutschalk A (2011): Potential fMRI correlates of 40-Hz phase locking in primary

839   auditory cortex, thalamus and midbrain. Neuroimage 54:495–504.

840   http://www.ncbi.nlm.nih.gov/pubmed/20688174.

841   Strom A, Iaccarino L, Edwards L, Lesman-Segev OH, Soleimani-Meigooni DN, Pham J, Baker

842   SL, Landau SM, Jagust WJ, Miller BL, Rosen HJ, Gorno-Tempini ML, Rabinovici GD, La

843   Joie R (2022): Cortical hypometabolism reflects local atrophy and tau pathology in

844   symptomatic Alzheimer's disease. Brain 145:713–728.

845   Sutton S, Braren M, Zubin J, E. R. John (1965): Evoked-Potential Correlates of Stimulus

846   Uncertainty. Science (80-) 150:1187–8.

847   Tarkka IM, Stokić DS, Basile LF, Papanicolaou a C (1995): Electric source localization of the

848   auditory P300 agrees with magnetic source localization. Electroencephalogr Clin

849   Neurophysiol 96:538–545.

850   Twomey DM, Murphy PR, Kelly SP, O'Connell RG (2015): The classic P300 encodes a build-to-

851   threshold decision variable. Eur J Neurosci 42:1636–43.

852   http://www.ncbi.nlm.nih.gov/pubmed/25925534.

853   Uutela K, Taulu S, Hämäläinen M (2001): Detecting and correcting for head movements in

854   neuromagnetic measurements. Neuroimage 14:1424–1431.

855   Verleger R, Heide W, Butt C, Kömpf D (1994): Reduction of P3b in patients with temporo-parietal

856   lesions. Brain Res Cogn Brain Res 2:103–116.

857   Verleger R (2020): Effects of relevance and response frequency on P3b amplitudes: Review of

858   findings and comparison of hypotheses about the process reflected by P3b.

859   Psychophysiology 57:1–22.

860   Verleger R, Metzner MF, Ouyang G, Śmigasiewicz K, Zhou C (2014): Testing the stimulus-to-

861   response bridging function of the oddball-P3 by delayed response signals and residue

862   iteration decomposition (RIDE). Neuroimage 100:271–280.

863   Vogt BA (2019): The cingulate cortex in neurologic diseases: History, Structure, Overview.

864   Handbook of Clinical Neurology 1st ed. Elsevier B.V. Vol. 166.

865   http://dx.doi.org/10.1016/B978-0-444-64196-0.00001-7.

866   Vogt BA, Nimchinsky EA, Vogt LJ, Hof PR (1995): Human cingulate cortex: Surface features, flat

867   maps, and cytoarchitecture. J Comp Neurol 359:490–506.

868   Vogt BA, Pandya DN (1987): Cingulate cortex of the rhesus monkey: II. Cortical afferents. J

869   Comp Neurol 262:271–289.

870   Yamaguchi S, Knight RT (1991): Anterior and posterior association cortex contributions to the

871   somatosensory P300. J Neurosci 11:2039–2054.

872   Yeo BTT, Krienen FM, Sepulcre J, Sabuncu MR, Lashkari D, Hollinshead M, Roffman JL, Smoller

873   JW, Zöllei L, Polimeni JR, Fisch B, Liu H, Buckner RL (2011): The organization of the

874   human cerebral cortex estimated by intrinsic functional connectivity. J Neurophysiol

875   106:1125–1165.

876   Ziontz J, Adams JN, Harrison TM, Baker SL, Jagust WJ (2021): Hippocampal connectivity with

877   retrosplenial cortex drives neocortical tau accumulation and memory function. J Neurosci

878   41:8839–8847.

879

880 ## Supporting information

881

882 ## A role for retro-splenial cortex in the task-related P3 network

883

884 **Diptyajit Das, Marnie E. Shaw, Matti S. Hämäläinen, Andrew R. Dykstra, Laura Doll, and**

885 **Alexander Gutschalk**
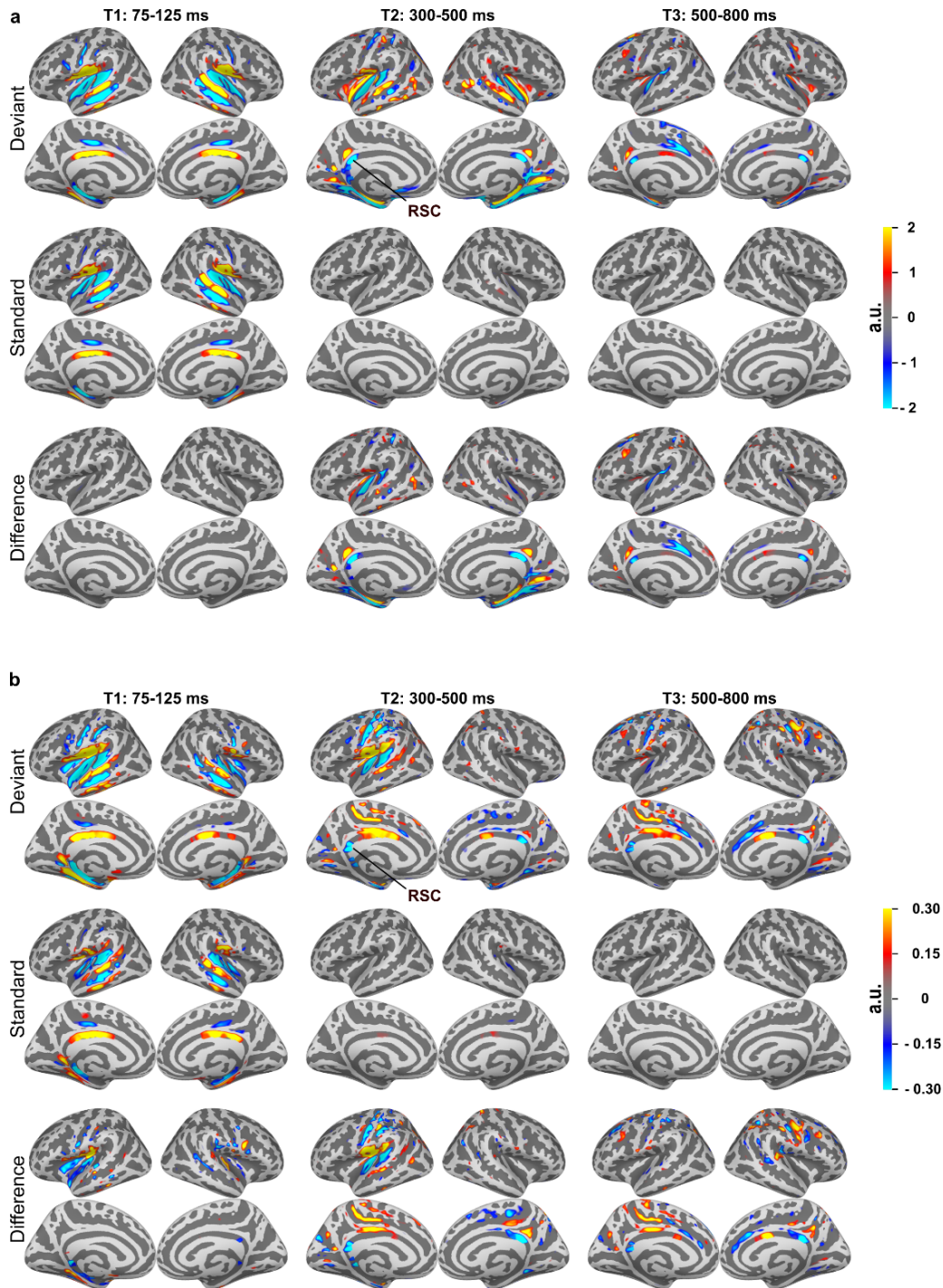
Figure S1 Cortical M/EEG and fMRI activation maps. These maps represent combined M/EEG source estimates similar to those shown in Figure 2a, but with alternative source analysis methods, using (a) sLORETA and (b) a Borgiotti-Kaplan beamformer. Note that the numerical values cannot be directly compared between these source estimation methods, even though they represent noise normalized z-scores.
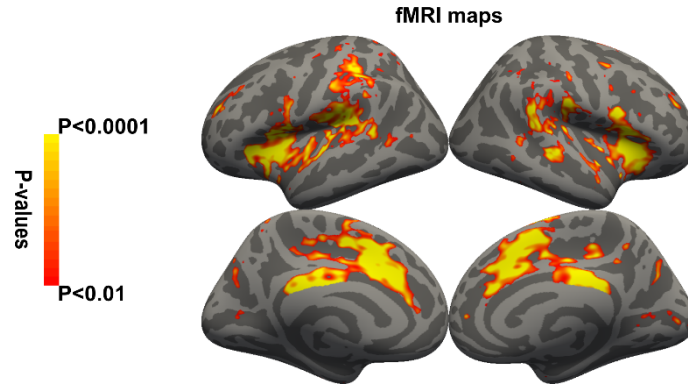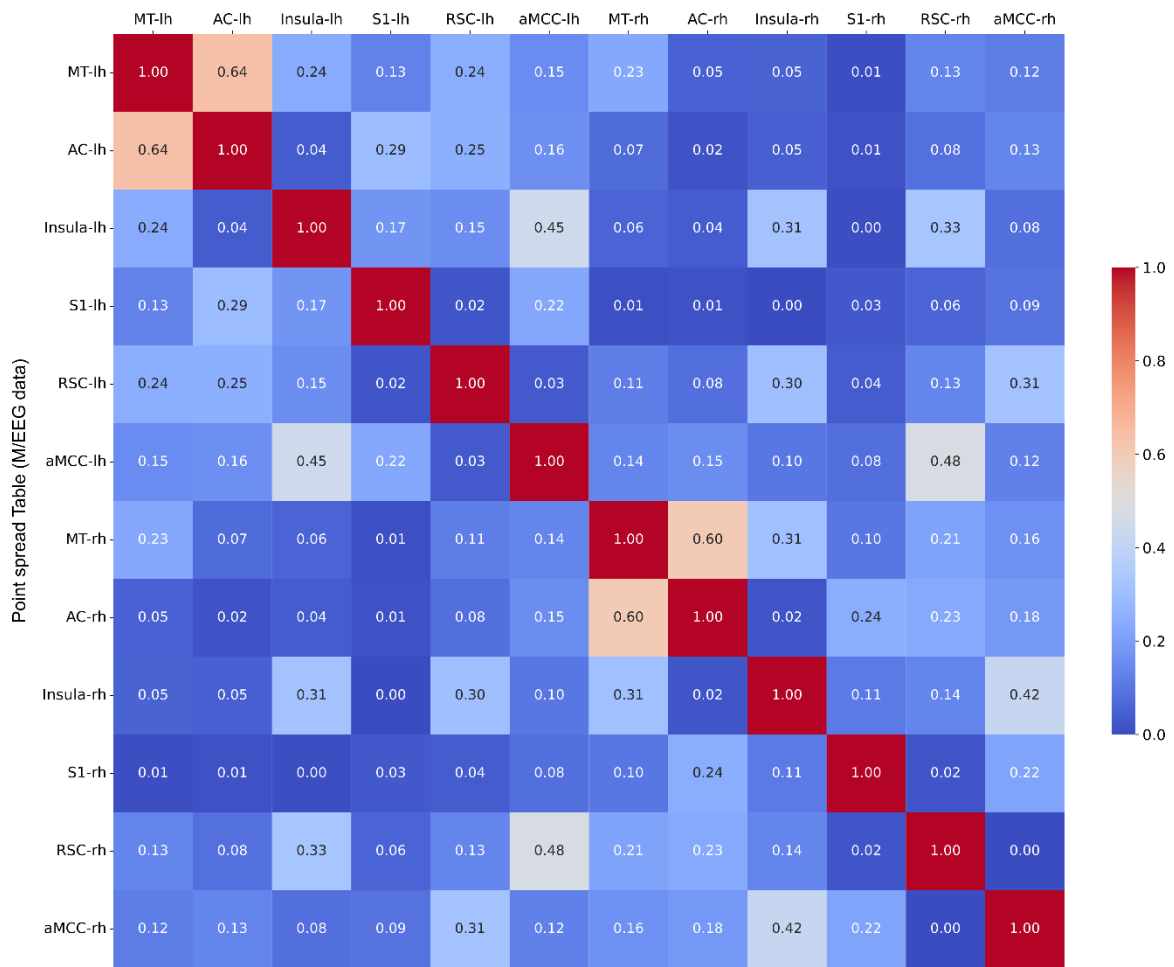
891

892 **Figure S2** fMRI maps for the contrast deviants – standards, based on a random-effects statistic.

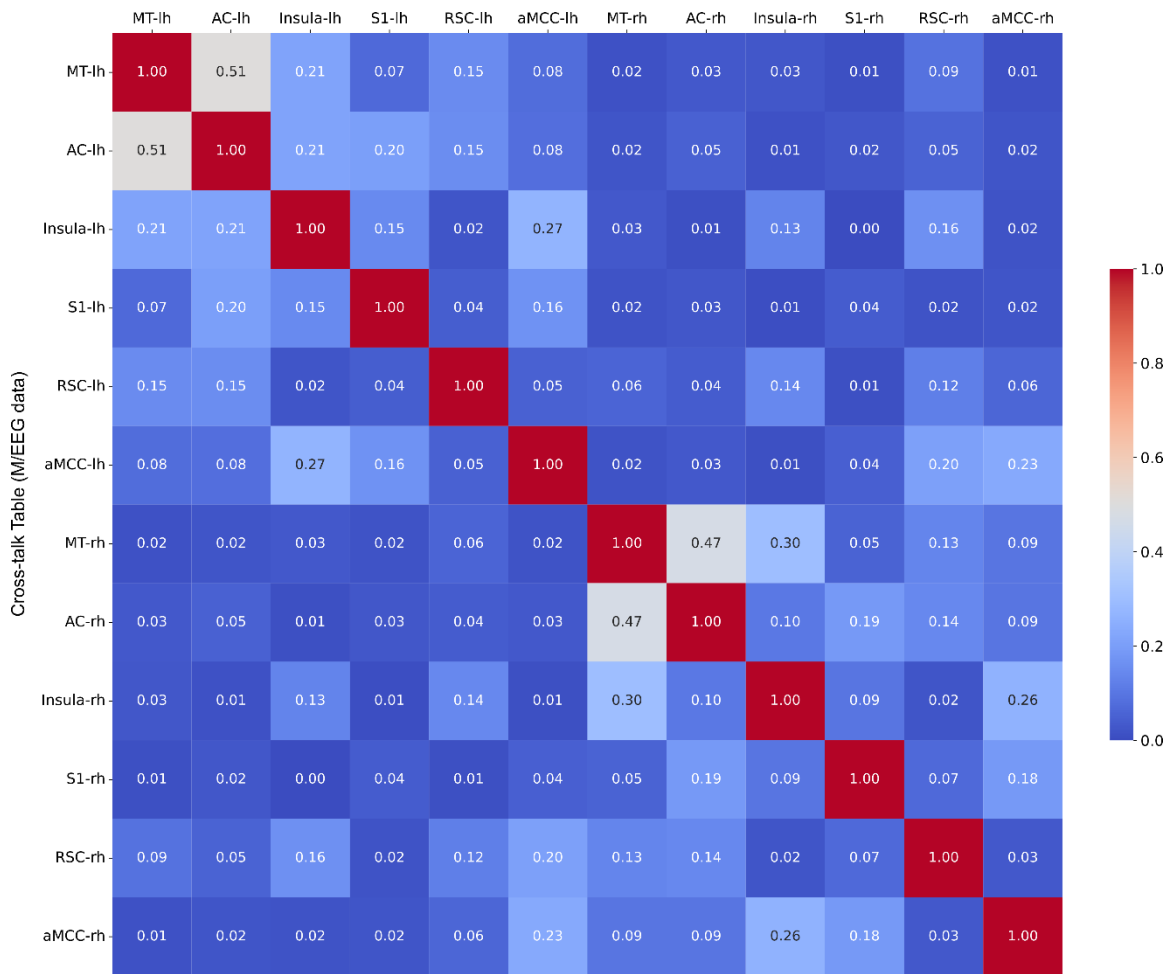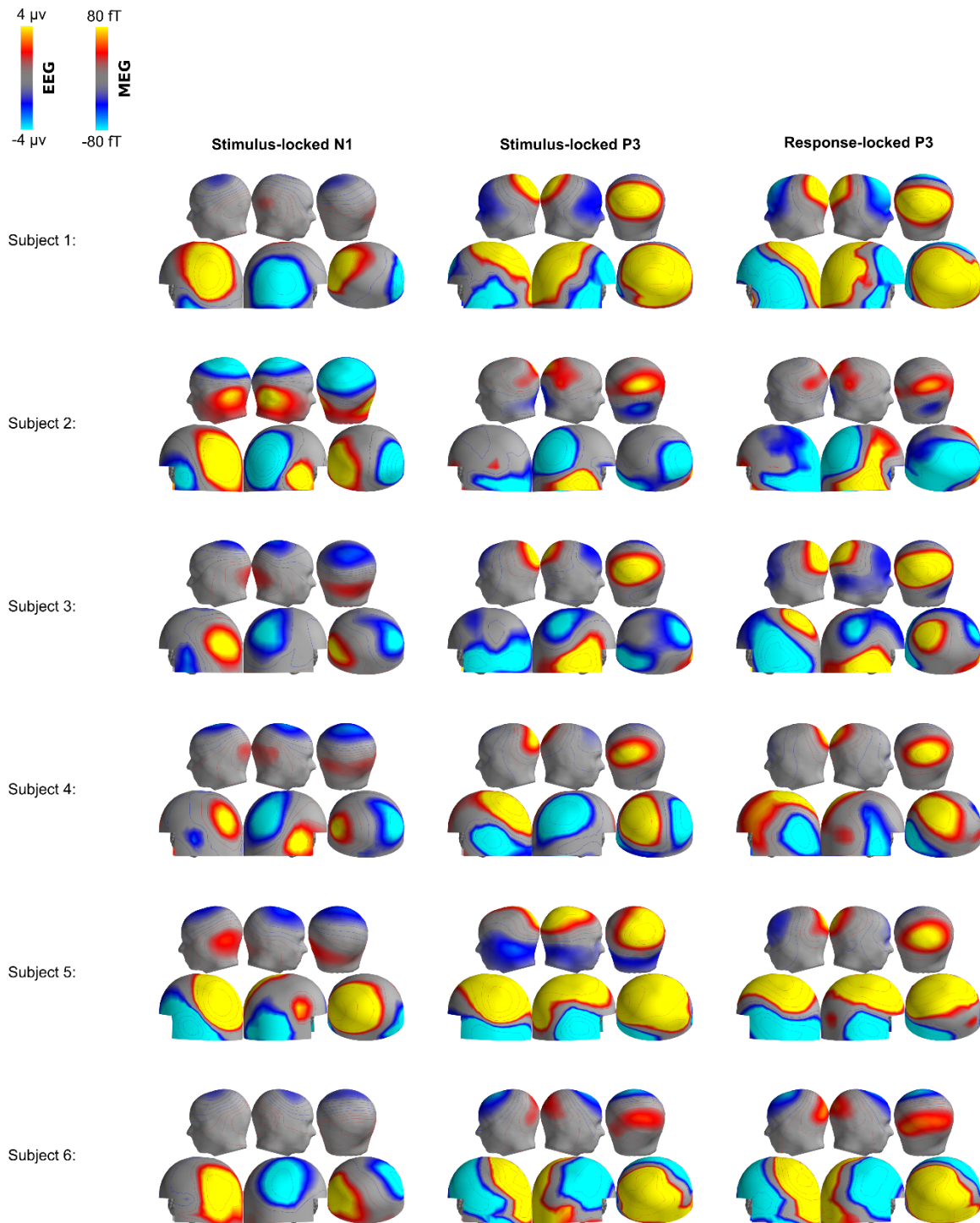893 Same analysis as Figure 2c but with more conservative cutoff (p<0.01, FDR corrected).

894

895

**Figure S3** Point spread analysis table based on the M/EEG data. The spread values range from 0 (minimum) to 1 (maximum).

Figure S4 Cross-talk analysis table based on the M/EEG data. The cross-talk values range from 0 (minimum) to 1 (maximum).

43

Figure S5 EEG and MEG maps for individual participants. The responses are mapped at the individual peak latency for N1 (left) stimulus-locked P3b (middle), and response-locked P3b (right) for individual participants 1 - 6.

905
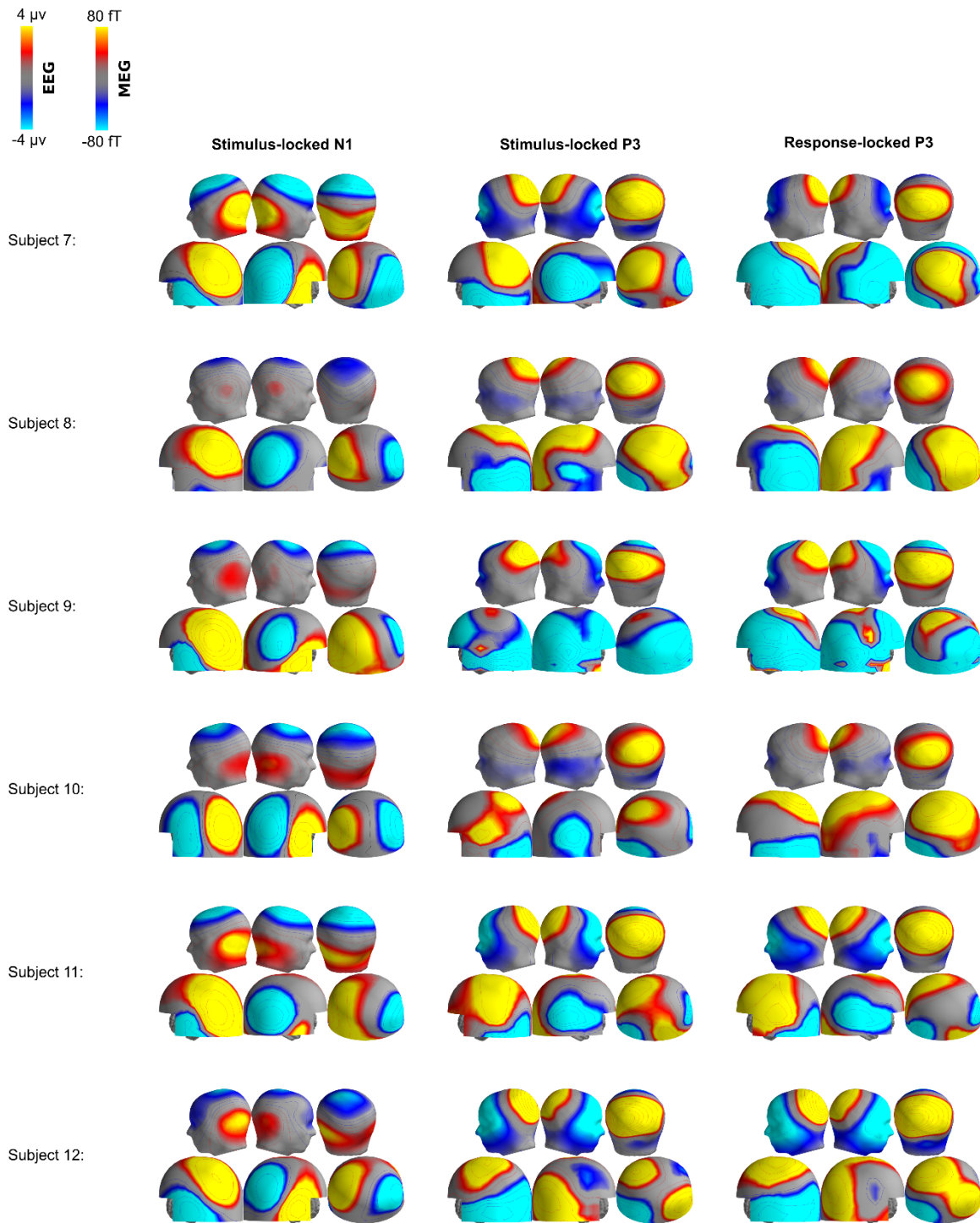
Figure S6 EEG and MEG maps for individual participants. The responses are mapped at the individual peak latency for N1 (left) stimulus-locked P3b (middle), and response-locked P3b (right) for individual participants 7 - 12.
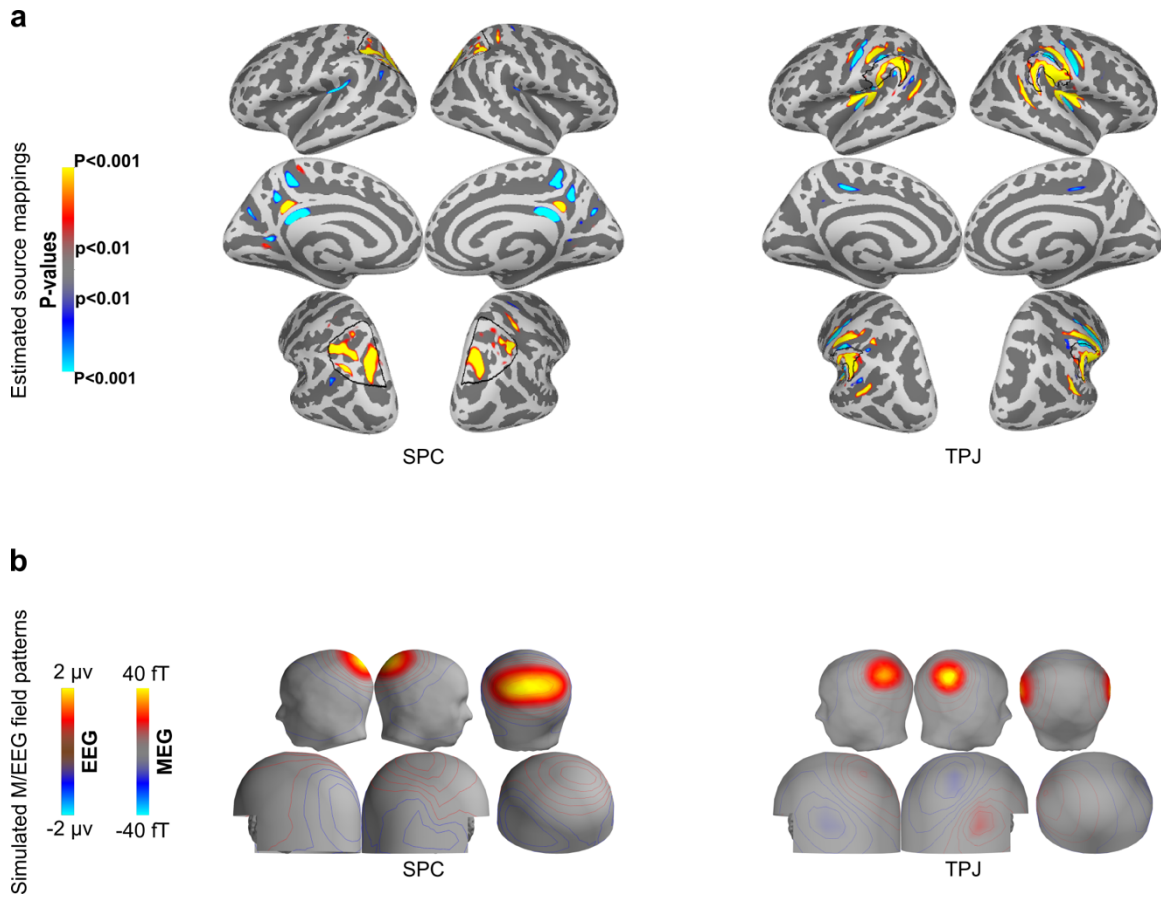
909

910   **Figure S7** Simulated M/EEG for a distributed superior parietal cortex (SPC) and a temporo-

911   parietal junction source (TPJ) source. (a) dSPM analysis for simulated distributed SPC (left) and

912   TPJ (right) sources (n=12 subjects; p<0.01). (b) Average EEG and MEG maps for the simulated

913   distributed SPC (left) and TPJ (right) sources.

914 **Table S1** Modeling the grand-average N1 pattern with simulated M/EEG based on anatomically

915 defined source regions (Figure 4b).

	Simulated source activation patterns					Residual variance (RV) (%)	
Source strength (nAm)	**AC**	**Insula**	**S1**	**RSC**	**aMCC**	**EEG**	**MEG**
	27.75	9.25	0.0	0.0	0.0	16.25	27.80
	28.75	-	-	-	-	20.70	26.80
	-	26.50	-	-	-	69.60	100.0

916

917   **Table S2** Modeling the grand-average P3b pattern with simulated M/EEG based on anatomically

918   defined source regions (Figure 4b). In this simulation, the extended superior parietal source (SPC;

919   see Figure S6) is used instead of the retro-splenial cortex (RSC).

	Simulated source activation patterns					Residual variance (RV) (%)	
	AC	**Insula**	**S1**	**SPC**	**aMCC**	**EEG**	**MEG**
Source strength (nAm)	5.0	11.25	10.0	69.50	0.	8.90	66.60
	-	7.25	11.75	66.25	6.50	8.80	70.30
	3.0	-	11.25	64.0	6.25	8.0	73.40
	9.0	16.0	-	79.0	0.	11.10	75.10
	0.	0.	22.75	-	4.0	52.90	87.10
	5.0	11.25	10.0	69.50	-	8.90	66.60

920